Proteomic analysis of the pyrenoid-traversing membranes of *Chlamydomonas reinhardtii* reveals novel components

Eric Franklin[1], Lianyong Wang[1], Edward Renne Cruz[1], Keenan Duggal[1], Sabrina L. Ergun[1,2], Aastha Garde[1,2], Alice Lunardon[1,2], Weronika Patena[1], Cole Pacini[1], Martin C. Jonikas[1,2]

[1]Department of Molecular Biology, Princeton University, Princeton, NJ 08544, USA
[2]Howard Hughes Medical Institute, Princeton University, Princeton, NJ 08544, USA

Summary

- Pyrenoids are algal CO_2-fixing organelles that mediate approximately one-third of global carbon fixation. Most pyrenoids are traversed by membranes that are thought to supply them with concentrated CO_2. Despite the critical nature of these membranes for pyrenoid function, they are poorly understood, with few protein components known in any species.
- Here, we identify protein components of the pyrenoid-traversing membranes from the leading model alga, *Chlamydomonas reinhardtii,* by affinity purification and mass spectrometry of membrane fragments. Our proteome includes previously-known proteins as well as novel candidates.
- We further characterize two of the novel pyrenoid-traversing membrane-resident proteins: Cre10.g452250, which we name Pyrenoid Membrane Enriched 1 (PME1), and Cre02.g143550, also known as Low-CO_2-Induced 16 (LCI16). We confirm the pyrenoid-traversing membrane localization of LCI16 and observe that PME1 and LCI16 physically interact. We find that neither protein is required for normal membrane morphology or growth under CO_2-limiting conditions, but that both mutants show a similar proteomic profile to those of established pyrenoid mutants.
- Taken together, our study identifies the proteome of the pyrenoid-traversing membranes and initiates the characterization of a novel pyrenoid-traversing membrane complex, building toward a mechanistic understanding of the pyrenoid.

Key words: Affinity purification, *Chlamydomonas reinhardtii*, CO_2-concentrating mechanism (CCM), mass spectrometry, membranes, membrane proteins, proteomics, pyrenoid

Introduction

Globally, photosynthetic organisms fix over 100 billion metric tons of carbon each year via the conserved enzyme Ribulose-1,5-bisphosphate carboxylase/oxygenase (Rubisco), thought to be the most abundant protein in the world (Ellis, 1979; Field *et al.*, 1998; Beardall & Raven, 2020). Despite its importance to the biosphere, Rubisco runs relatively slowly for an enzyme in central carbon metabolism and is prone to catalyzing oxygenation, a wasteful reaction with oxygen (Flamholz *et al.*, 2019). Some organisms overcome these limitations through the use of CO_2-concentrating mechanisms (CCMs). These mechanisms improve the efficiency of carbon fixation by concentrating CO_2 locally around Rubisco to increase its rate of carboxylation and decrease unwanted oxygenation (Hatch, 1987; Lüttge, 2004; Sage *et al.*, 2012; Raven *et al.*, 2017).

Eukaryotic algae, which mediate most of the CO_2 assimilation in the oceans (Mackinder, 2017), nearly all use a CCM based on a chloroplast-localized organelle called the pyrenoid (Wang *et al.*, 2015; Beardall & Raven, 2020; Meyer *et al.*, 2020a; Barrett *et al.*, 2021; He *et al.*, 2023). A pyrenoid is formed by tightly clustering the cell's Rubisco into a biomolecular condensate (Freeman Rosenzweig *et al.*, 2017). Concentrated CO_2 is released inside this condensate, increasing the carboxylation rate of Rubisco and decreasing its oxygenation. Despite their importance to the global carbon cycle, pyrenoids remain understudied and poorly understood at a molecular level.

Because pyrenoids evolved many times across independent algal lineages (Meyer *et al.*, 2020a; Barrett *et al.*, 2021; He *et al.*, 2023), many of the specific genes involved in CCM function differ between phylogenetic groups. However, we expect that common principles of biogenesis and function underlie these convergently-evolved structures. Our approach to uncovering these principles is to study the leading model alga, *Chlamydomonas reinhardtii* (*C. reinhardtii* hereafter), whose pyrenoid is currently best understood. The existence of an extensive experimental toolbox in this organism—including well-defined genetic and proteomic protocols and a library of knockout mutants—makes it a powerful platform for the discovery and characterization of novel pyrenoid components.

The *C. reinhardtii* pyrenoid consists of a phase-separated matrix containing tightly-packed Rubisco (Freeman Rosenzweig *et al.*, 2017), and is surrounded by a starch sheath that appears to limit CO_2 leakage and is required for normal localization of CCM components (Toyokawa *et*

66 *al.*, 2020; Fei *et al.*, 2022). Traversing the matrix are specialized membranes that are thought to
67 mediate the delivery of concentrated CO_2 to the matrix (Raven, 1997; Karlsson *et al.*, 1998;
68 Sinetova *et al.*, 2012; Fei *et al.*, 2022).
69
70 In *C. reinhardtii*, the pyrenoid-traversing membranes form a network of tubules that is
71 contiguous with but ultrastructurally distinct from the photosynthetic thylakoid membranes
72 (Engel *et al.*, 2015). Tubules are constitutively present, including during cell division
73 (Goodenough, 1970), in non-CCM-requiring growth conditions (Ma *et al.*, 2011; Caspari *et al.*,
74 2017), and in mutants deficient in pyrenoid matrix formation (Goodenough & Levine, 1970; Ma
75 *et al.*, 2011; Mackinder *et al.*, 2016; Caspari *et al.*, 2017; He *et al.*, 2020). The tubules are
76 structurally complex, being composed of a central reticulated region with narrow tubules
77 interconnected by three-way junctions, larger cylindrical tubules which extend radially out
78 toward the pyrenoid periphery, and smaller minitubules within the cylindrical tubules that also
79 appear to be made of membranes (Engel *et al.*, 2015). The tubule network is dynamic, with
80 tubule quantity and diameter varying under different growth conditions (Rawat *et al.*, 1996).
81 Given the presence of the tubules in the absence of a pyrenoid matrix, it has been proposed
82 that they play an organizational role in pyrenoid nucleation or localization (Meyer *et al.*, 2020b),
83 while their presence in non-CCM-requiring growth conditions suggests possible additional
84 functions beyond CO_2 delivery.
85
86 To date, several tubule-localized proteins have been identified with varying degrees of
87 confidence. The best-established proteins that localize specifically to the tubules are Carbonic
88 AnHydrase 3 (CAH3; Cre09.g415700), which is thought to deliver CO_2 to the pyrenoid (Karlsson
89 *et al.*, 1998; Sinetova *et al.*, 2012); MIssing THylakoids 1 (MITH1; Cre06.g259100), which is
90 necessary for producing pyrenoid-traversing membranes (Hennacy *et al.*, 2024); and Rubisco-
91 Binding Membrane Proteins 1 and 2 (RBMP1, Cre06.g261750; RBMP2, Cre09.g416850) (Meyer
92 *et al.*, 2020b). The functions of RBMP1 and RBMP2 are not fully understood, though RBMP1,
93 also known as BST4, shares homology with the thylakoid-localized putative bicarbonate
94 transporters BST1-3 (Mukherjee *et al.*, 2019) and impacts tubule lumen pH during dark-to-light
95 transition, possibly by mediating bicarbonate transport across the tubule membrane (Adler *et al.*,
96 2024).
97
98 Multiple strategies have been employed to isolate and identify *C. reinhardtii* pyrenoid proteins,
99 including fractionation of whole pyrenoids (Mackinder *et al.*, 2016; Zhan *et al.*, 2018), systematic

protein localization and affinity purification of protein complexes using known pyrenoid components as baits (Mackinder, 2017; Wang *et al.*, 2023), and proximity labeling of pyrenoid proteins using TurboID (Lau *et al.*, 2023). However, none of these methods were explicitly focused on the pyrenoid tubules.

Here, we identify tubule-localized proteins by developing a complementary approach that relies on enriching fragments of pyrenoid-traversing membranes. This approach adapts an existing affinity purification method (Wang *et al.*, 2023) to isolate membrane fragments rather than protein complexes, similar to previous methods for purifying intact organelles and membrane fractions (Zhang *et al.*, 2007; Chen *et al.*, 2016; Yao *et al.*, 2018; Chen *et al.*, 2022). We show that our method successfully recovers known tubule proteins and identifies novel candidates. We further validate and characterize two of the top candidates. By expanding the known pyrenoid tubule proteome, this work contributes to paving the way toward a mechanistic understanding of pyrenoid function.

Materials and Methods

Strains and Culture Conditions

All insertional mutants were obtained from the CLiP collection at the Chlamydomonas Resource Center (Li *et al.*, 2019) or from the recently-reported CLiP2 mutant collection (Lunardon *et al.*, 2024). Mutant IDs for these strains and their wild-type background strains can be found in Table **1** below. All strains generated in this work were deposited to the Chlamydomonas Resource Center (https://chlamycollection.org).

Unless otherwise noted, cultures were grown in TP media to a concentration of ~1-2×10^6 cells mL^{-1} prior to experiments. Unless otherwise noted, cultures were grown in low CO_2 (air, ~0.04% v/v CO_2) and 150 μmol · m^{-2} · s^{-1} photons.

Table 1. **Strains used in this work**

Chlamydomonas Resource Center ID	Strain Description	Mating Type	Source	Antibiotic Resistance
CC-4533	Wild type CMJ030	*mt(-)*	Wild type; parent strain to CLiP library (Zhang *et al.*, 2014)	none

CC-5415	Wild type	*mt(+)*	Wild type; parent strain to *lci16-2 and lci16-3* (Lunardon *et al.*, 2024)	none
CC-5646	CMJ030;RBMP1-Venus-3×FLAG	*mt(-)*	Previously published	Paromomycin
CC-5647	CMJ030;RBMP2-Venus-3×FLAG	*mt(-)*	Previously published	Paromomycin
CSI_LW07G9	CMJ030;CPLD9-Venus-3×FLAG	*mt(-)*	CSI collection (Meyer *et al.*, 2020b; Wang *et al.*, 2023)	Paromomycin
CSI_LW01C3	CMJ030;CGL129 -Venus-3×FLAG	*mt(-)*	CSI collection (Wang *et al.*, 2023)	Paromomycin
CC-6234	CMJ030;LCI16-Venus-3×FLAG	*mt(-)*	CMJ030 transformed with pLM005-LCI16-Venus-3×FLAG	Paromomycin
LMJ.RY0402.141937	*pme1-1*	*mt(-)*	CLiP library (Li *et al.*, 2019)	Paromomycin
LMJ.RY0402.168140	*pme1-2*	*mt(-)*	CLiP library (Li *et al.*, 2019)	Paromomycin
LMJ.RY0402.236076	*pme1-3*	*mt(-)*	CLiP library (Li *et al.*, 2019)	Paromomycin
LMJ.RY0402.215307	*lci16-1*	*mt(-)*	CLiP library (Li *et al.*, 2019)	Paromomycin
CLIP2.000095	*lci16-2*	*mt(+)*	CLiP2 library (Lunardon *et al.*, 2024)	Hygromycin
CLIP2.000923	*lci16-3*	*mt(+)*	CLiP2 library (Lunardon *et al.*, 2024)	Hygromycin

Membrane Affinity Purification and Mass Spectrometry

Detergent-based affinity purification and mass spectrometry of RBMP1-Venus-3×FLAG, RBMP2-Venus-3×FLAG, and LCI16-Venus-3×FLAG were performed as described previously (Wang *et al.*, 2023).

For the membrane affinity purification, our objective was to isolate fragments of membranes of interest. We sought to achieve this by choosing baits localized to our membranes of interest and performing a standard affinity purification, as described in (Wang *et al.*, 2023), but with the membrane disruption step changed from dissolution with detergent to shearing with sonication. We used two tubule bait proteins (RBMP1 and RBMP2) and two thylakoid bait proteins (CPLD9, Cre01.g005001; CGL129, Cre05.g233950) (Meyer *et al.*, 2020b; Wang *et al.*, 2023). Each bait protein was expressed in an independent strain in the CMJ030 (CC-5433) wild-type background. We performed three iterations of this membrane affinity purification experiment, each with slight differences meant to better enrich membranes or better detect the proteins enriched in the purification.

145

146 The membrane affinity purification was based on the protocol previously described in (Wang *et*
147 *al.*, 2023). Each strain expressing a FLAG-tagged protein was pre-cultured in 5 mL TAP media
148 + 2 µg/mL paromomycin under ~100-150 µmol · m^{-2} · s^{-1} photons until reaching a concentration
149 of ~2-4×10^6 cells mL^{-1}. 1 mL of each of these cultures was used to inoculate 50 mL of TAP + 2
150 µg/mL paromomycin and grown again under ~100-150 µmol · m^{-2} · s^{-1} photons until reaching a
151 concentration of ~2-4×10^6 cells mL^{-1}. These cultures were then centrifuged at 1,000×g for 5
152 minutes, resuspended in 50 mL TP + 2 µg/mL paromomycin, and transferred to a 1L bottle
153 containing 800 mL of TP + 2 µg/mL paromomycin. These cultures were bubbled with air at
154 ~150-200 µmol · m^{-2} · s^{-1} photons until reaching a density of ~2-4×10^6 cells mL^{-1}. Cells were
155 harvested by centrifugation at 4°C for 10 minutes at 3,000×g, washed in 40 mL of ice-cold 1×IP
156 buffer (25 mM HEPES, 25 mM KOAc, 1 mM $Mg(OAc)_2$, 0.5 mM $CaCl_2$, 100 mM Sorbitol, 1mM
157 NaF, 0.3 mM Na_3VO_4, and cOmplete EDTA-free protease inhibitor (1 tablet/500 mL)) then
158 pelleted at 4°C for 10 minutes at >3,000×g. Importantly, to keep membranes intact, our IP buffer
159 did not include digitonin, in contrast to the IP buffer used in Wang, et al. Pellets were weighed
160 and resuspended in a 1:1 (v/w) ratio of ice-cold 2×IP buffer, and the resulting cell suspension
161 was then dripped into liquid nitrogen to form small popcorn pellets which were stored at -80°C.
162 Cells were broken open by grinding for 20 minutes with a Cryomiller under liquid nitrogen
163 temperatures, and the resulting powder was defrosted on ice for at least 45 minutes and
164 dounced 20 times in a pre-chilled Kontes Glass Col. Duall #22 Douncer (Kimble). Rather than
165 dissolving membranes using IP buffer with digitonin and centrifuging at 12,700×g, as in the
166 Wang et al. protocol, membranes were instead disrupted by sonicating with a probe sonicator
167 (QSonica) in 20 cycles of (5 x 1 sec. pulse at 40% amplitude, 30 sec. rest) in a microcentrifuge
168 tube on ice. Following sonication, lysate was clarified by centrifugation at 1,000×g for 30
169 minutes at 4°C to remove cellular debris. 750 µL of the supernatant containing the membrane
170 fragments was incubated with Anti-FLAG M2 Magnetic Beads (Sigma) that had been pre-
171 washed twice with 1 mL 1×IP buffer and thrice with 1×IP buffer plus 0.1% digitonin (twice with 1
172 mL and once with 150 µL). The membrane fragment–containing lysate was nutated with the
173 Anti-FLAG beads for 1.5 hours at 4°C, washed four times by nutating for 2 minutes in 1×IP
174 buffer, and eluted for 30 minutes at 4°C with 5 µg $µL^{-1}$ 3×FLAG peptide in 1×IP buffer plus 5%
175 digitonin. Note that the concentrations of FLAG peptide and digitonin are higher in our elution
176 step than in the elution step of the original Wang et al protocol. These were included in order to
177 compensate for the higher avidity of membrane fragments bearing multiple FLAG-tagged
178 proteins compared to the individual protein complexes immunoprecipitated in the original

179 protocol, as well as to dissolve the membrane fragments before moving on to protein
180 identification by mass spectrometry.
181
182 After elution, samples were denatured by heating at 70°C for 10 minutes, then were loaded into
183 a 4-20% Criterion TGX Precast Mini Protean Gel (BioRad) for electrophoresis at 50 V for 40 min
184 until the protein front moved ~2.0 cm to separate the FLAG peptides from the eluted proteins.
185 Each lane was cut from below the bottom of the well to just below the bottom of the ladder (~5
186 kDa) and gel slices were stored at 4°C until processing for in-gel digestion. Samples were
187 loaded in every other well to decrease cross-contamination between samples. Mass
188 spectrometry was performed as described in (Wang *et al.*, 2023). The results of this membrane
189 affinity purification experiment are represented in Fig. **2a** and full results can be found in
190 Supporting Information Dataset **S1**.
191
192 The second affinity purification replicated the first with the following changes: 1) sonication was
193 performed using 6 cycles of (10s at 80% amplitude, 20s rest) on ice; 2) sonicated lysate was
194 clarified at 5,000×g instead of 1,000×g; 3) In place of elution with FLAG peptide and in-gel
195 digestion of proteins, proteins were digested on-bead using S-Trap™ Micro Spin Column
196 Digestion (Protifi); 3) Samples were run on the mass spectrometer for 2 hours instead of 1 hour.
197 The results of this membrane affinity purification experiment are represented in Fig. **2b** and full
198 results can be found in Supporting Information Dataset **S2**.
199
200 The third affinity purification was performed like the first with the following changes: 1)
201 sonication was performed using 6 cycles of (10s at 80% amplitude, 20s rest) on ice; 2)
202 sonicated lysate was centrifuged at 5,000×g; 3) after elution, samples were frozen in liquid
203 nitrogen and submitted to the Thermo Fisher Scientific Center for Multiplexed Proteomics at
204 Harvard Medical School for digestion, tandem mass tag (TMT) labeling (Thermo Fisher), and
205 quantitative mass spectrometry (Ting *et al.*, 2011; McAlister *et al.*, 2012; Li *et al.*, 2020). The
206 results of this membrane affinity purification experiment are represented in Fig. **2c** and full
207 results can be found in Supporting Information Dataset **S3**.
208
209 **Live-Cell Imaging**
210 For live-cell imaging, strains expressing Venus-tagged proteins were grown at 3% CO_2 in TP
211 media to a concentration of ~5×10^5 cells mL^{-1}, then transferred to ambient CO_2 16 hours before
212 collecting for imaging at a concentration of ~$1\text{-}2\times10^6$ cells mL^{-1}. 200 µL of each cell culture were

213 placed into the wells of an 8-well μ-slide (Ibidi) and allowed to settle for 5 minutes. The culture
214 media was aspirated to leave a thin layer of cells, and the cells were immobilized for imaging by
215 flowing over 1 mL of 2% low-melting-point TP agarose in each well at ~40°C, which was allowed
216 to set for 5 minutes at room temperature prior to imaging.
217
218 Cells were imaged using a VT-iSIM super-resolution spinning-disk confocal microscope on an
219 Olympus iX83 body equipped with VisiView software, a 60X 1.43 NA objective and a
220 Hamamatsu Orca Quest sCMOS camera in slow mode. Venus fluorescence was excited using
221 a 514 nm laser and collected at 545/50 nm. Chlorophyll autofluorescence was excited using a
222 642 nm laser and collected at 700/75 nm. Confocal Z-series were acquired with a 300 nm Z-
223 step. The same acquisition settings were used for all strains imaged in this study. Images were
224 imported into Fiji (Schindelin *et al.*, 2012) for deconvolution using the Microvolution plugin and
225 final image preparation.
226
227 **Transmission Electron Microscopy (TEM)**
228 TEM was performed as described in (He *et al.*, 2020) with some modifications. Strains for TEM
229 imaging were grown at 3% CO_2 in TP media to a concentration of ~5×10^5 cells mL^{-1}, then
230 transferred to ambient CO_2 16 hours before harvesting at a concentration of ~$1\text{-}2\times10^6$ cells mL^{-}
231 ^{1}. At least 50×10^6 cells were harvested by centrifugation at 1,000×g for 5 minutes in 50 mL
232 tubes, resuspended in 1 mL TP, transferred to 1.5 mL screw-top tubes, and centrifuged again
233 for 5 minutes at 1,000 x g. Cells were then resuspended in 2.5% gluteraldehyde in TP media
234 (10 mL 10% gluteraldehyde, 30 mL TP) and nutated at room temperature for 1 hour. After
235 nutation, cells were pelleted at 3,000×g for 1 minute, then washed 3 times by resuspending and
236 nutating in 1 mL ddH_2O for 5 minutes each, pelleting at 3,000×g after each wash. Samples were
237 then post-fixed and stained with 1 mL freshly-prepared osmium tetroxide solution (1% OsO_4,
238 1.5% w/v $K_3[Fe(CN)_6]$, 2 mM $CaCl_2$) and nutated for 1-2 hours. Tubes were wrapped in
239 aluminum foil during nutation to protect samples from light. Counterstaining with uranyl acetate
240 was found to increase background staining and reduce contrast when looking at membranes, so
241 for all images shown and analyzed here, OsO_4 was the only stain used. Samples were then
242 serially dehydrated by resuspension and nutation in increasing concentrations of ethanol: 5
243 minutes in 1 mL each of 30%, 50%, 70%, and 95% ethanol, then 10 minutes in 100% ethanol
244 and 2×10 minutes in 100% acetonitrile. Samples were pelleted for 1 minute at 3,000×g between
245 each resuspension.
246

247 After dehydration, samples were embedded in epoxy resin containing 34% Quetol 651, 44%
248 nonenyl succinic anhydride, 20% methyl-5-norbornene-2,3-dicarboxylic anhydride and 2%
249 catalyst dimethylbenzylamine (Electron Microscopy Sciences) over four days, first by
250 embedding overnight in 1:1 acetonitrile:resin (no catalyst) with the screw-top tube open in a
251 fume hood, then by nutating in 1 mL Quetol resin (including catalyst) for four days, spinning
252 down the samples and resuspending in fresh resin once per day. On day 4, the samples were
253 resuspended in 300-500 µL resin, centrifuged at max speed (18,213 x g) for 20 minutes at 30°C
254 in a tabletop centrifuge with a swinging bucket rotor for microfuge tubes, then cured at 60–65°C
255 for 48 hours.
256
257 Thin (~70 nm) sections were prepared from cured resin blocks on a Leica Microtome Ultracut
258 UCT and mounted on carbon film–coated 200 mesh copper TEM grids (Electron Microscopy
259 Sciences) and imaged at the Imaging and Analysis Center, Princeton University, using a CM200
260 TEM (Philips) or a Talos F200X STEM (ThermoFisher Scientific).
261
262 **Growth assays**
263 Cells were grown in liquid TP media at high CO_2 (~3%) to a concentration of ~1-2×10^6 cells mL^{-}
264 ^{1}, then harvested by centrifugation by at 1,000×g for 5 minutes. Cultures were resuspended at a
265 density of 6×10^6 cells mL^{-1}, diluted 1:10 and 1:100, and spotted in 5 µL spots onto TP agar.
266 Plates were incubated in 3%, ~400 ppm, or ~50 ppm CO_2 and under 100 or 300 µmol · m^{-2} · s^{-1}
267 photons. Plates were imaged after 6 days using a Phenobooth (Singer Instruments).
268
269 **Immunofluorescence Staining and Imaging**
270 Immunostaining and imaging were performed as described previously (Yamano & Fukuzawa,
271 2016). Briefly, cells were centrifuged, washed twice with PBS, and applied to Poly-L-Lysine
272 coated glass slides. Cells were permeabilized with PBS-T and fixed with 4% formaldehyde.
273 Cells were further fixed in 100% ice-cold methanol, except for experiments in which chlorophyll
274 was retained. Cells were rehydrated with PBS, blocked, and stained with α-LCI16 (Yenzym), α-
275 RBMP1 (obtained from the Mackinder Lab; (Adler *et al.*, 2024)), or α-FLAG (Cell Signaling
276 8146T) primary antibodies at a 1:500 dilution. Cells were then washed with PBS-T and stained
277 Goat anti-Rabbit IgG (H+L) Secondary Antibody cross-adsorbed with Alexa Fluor 488
278 (Invitrogen A-11008) or Alexa Fluor 564 (Invitrogen A-11035), or with F(ab')2-Goat anti-Mouse
279 IgG (H+L) Secondary Antibody cross-adsorbed to Alexa Fluor 488 (Invitrogen A-11017). Cells
280 were imaged using a VT-iSIM super-resolution spinning-disk confocal microscope on an

281 Olympus iX83 body equipped with VisiView software, a 100x NA 1.35 silicone immersion
282 objective, and a Hamamatsu Orca Quest sCMOS camera in slow mode.
283
284 **Whole-cell proteomics**
285 For whole-cell proteomics, strains were inoculated from fresh TAP plates into 15 mL TAP liquid
286 cultures and grown in air at ~150 μmol · m^{-2} · s^{-1} to a concentration of ~1-2×10^6 cells mL^{-1}.
287 These cultures were used to inoculate 50 mL TP liquid cultures at a density of ~2.5-5×10^5 cells
288 mL^{-1} and grown at high CO_2 (~3%) at ~150 μmol · m^{-2} · s^{-1} to a concentration of ~1-2×10^6 cells
289 mL^{-1}. The high CO_2 cultures were finally used to inoculate 200 mL TP liquid cultures at a density
290 of ~2.5-5×10^5 cells mL^{-1}, which were grown at low CO_2 (~400 ppm) and ~150 μmol · m^{-2} · s^{-1} for
291 16 hours. Cultures were harvested by centrifugation at 1,000×g and washed three times in PBS.
292 The pellets after the last PBS wash were frozen in liquid nitrogen and stored at -80°C. Samples
293 were then submitted to the Thermo Fisher Scientific Center for Multiplexed Proteomics at
294 Harvard Medical School for digestion, tandem mass tag (TMT) labeling, and quantitative mass
295 spectrometry. Samples were processed as follows: 25 µg of protein from each sample was
296 reduced with TCEP, alkylated with iodoacetamide, and further reduced with DTT. Proteins were
297 precipitated onto SP3 beads to facilitate a buffer exchange into digestion buffer, digested with
298 Lys-C (1:50) overnight at room temperature and with trypsin (1:50) for 6 hours at 37°C, and
299 labelled with TMT 18plex reagents. 2 µL of each sample was pooled and used to shoot a ratio
300 check to confirm complete TMT labelling, and samples were pooled according to the ratios
301 determined by the ratio check. Peptides were desalted using a Sep-pak and fractionated using
302 basic reverse phase HPLC. Six fractions were solubilized, desalted by stage tip, and analyzed
303 on an Orbitrap Fusion Lumos. Peptide spectral matches were filtered to a 1% false discovery
304 rate (FDR) using the target-decoy strategy combined with linear discriminant analysis. The
305 proteins were filtered to a <1% FDR and quantified only from peptides with a summed SN
306 threshold of >180. Comet Search Parameters were as follows: Peptide Mass Tolerance: 50
307 ppm, Fragment Ion Tolerance: 1.0005, Fragment Bin Offset: 0.4, Theoretical Fragment Ions: 1,
308 Max Internal Cleavage Site: 2, Max differential/Sites: 5, methionine oxidation are used as
309 variable modification. MT Reporter Quant Parameters were as follows: Proteome (MS#) -
310 tolerance = 0.003, ms2 isolation width = 0.7, ms3 isolation width = 1.2. We note that PME1
311 levels in the *pme1* mutants appear unchanged from wild type; we believe this is due to very low
312 absolute levels of PME1 in wild type preventing accurate quantification. This is supported by the
313 peptide-level quantification, in which PME1 peptide levels were detected at similarly low levels
314 as EPYC1, MITH1, and SAGA1 peptides were detected in their respective mutants, indicating

315 that PME1 peptide levels in both wild-type and the *pme1* mutant strains are low enough that
316 they likely represent noise.
317

318 Results

319 **Isolation of membrane fragments using affinity purification**

320 The use of affinity purification to identify protein complexes is well-documented (Morris *et al.*,
321 2014; Meyer & Selbach, 2015). Such methods usually involve the use of detergents during cell
322 lysis to dissolve membranes (Behnke & Urner, 2023), such that proteins co-precipitate with the
323 bait protein only if they are part of the same protein complex. This strategy has been used to
324 identify novel protein complexes and elucidate functions for previously uncharacterized genes in
325 *C. reinhardtii* (Mackinder, 2017; Wang *et al.*, 2023). However, here we wanted to isolate
326 fragments of tubule membrane to comprehensively identify pyrenoid tubule-localized proteins in
327 an unbiased fashion.
328

329 We therefore adapted an existing affinity purification protocol used in *C. reinhardtii* (Mackinder,
330 2017; Wang *et al.*, 2023) to affinity purify intact membrane fragments. Using tagged membrane
331 proteins of known localization (Fig. **1a**) as bait, we performed the affinity purification protocol on
332 cell lysate in which membranes were disrupted by sonication rather than solubilized by
333 detergent (Fig. **1b**). We reasoned that this approach would produce membrane fragments that
334 would allow the identification of proteins that co-localized to the same membrane regions, even
335 if they do not directly interact (Fig. **1c**).
336

337 We selected four bait proteins on which to perform this protocol: RBMP1-Venus-3×FLAG and
338 RBMP2-Venus-3×FLAG (Fig. **1d,e**), which localize to the pyrenoid tubules (Meyer *et al.*, 2020b);
339 and CPLD9-Venus-3×FLAG and CGL129-Venus-3×FLAG (Fig. **1f,g**), which localize to the
340 thylakoid membranes and are excluded from the tubules (Wang *et al.*, 2023). RBMP1 and
341 RBMP2 localize to distinct regions of the tubules—RBMP1 to the tubule periphery and RBMP2
342 to the central reticulated region (Meyer *et al.*, 2020b, Supporting Information Fig. **S1**)—thus, we
343 reasoned that together they should provide coverage for the whole tubule network. As expected
344 from their distinct localizations, RBMP1 and RBMP2 did not co-precipitate via traditional
345 detergent-based affinity purification (Fig. **1h**, Supporting Information Dataset **S4**).
346

347 **A membrane affinity purification–based tubule proteome identifies known and novel**
348 **proteins**

349 We performed three iterations of the membrane affinity purification experiment, each with slight
350 modifications to the protocol to try and improve the enrichment or identification of membrane
351 proteins. Samples from the first two experiments were quantified using label-free quantification
352 (LFQ), identifying 58 and 135 proteins, respectively, that were at least 2-fold enriched in the
353 tubule samples relative to the control samples (Fig. **2a-b**, Supporting Information Datasets **S1–**
354 **2**). Quantification using LFQ, however, can suffer from Poisson noise for lower-abundance
355 proteins, leading some low-abundance proteins to appear enriched or depleted in a given
356 sample due to differences in random run-to-run peptide sampling rather than differences in
357 actual abundance in each sample (O'Connell *et al.*, 2018). We therefore set a minimum
358 abundance threshold for proteins to be considered hits in those experiments, which reduced the
359 number of 2-fold-enriched hits in the first two experiments to 22 and 92, respectively. To further
360 address the problem of noisy results for low-abundance proteins, the third iteration of the
361 membrane purification experiment used tandem mass tag (TMT) labeling instead of LFQ. TMT
362 labelling allows all samples to be multiplexed and run simultaneously, so that any random
363 sampling of low-abundance peptides applies to all samples equally, leading to more accurate
364 quantification of lower-abundance proteins and obviating the need for a minimum abundance
365 threshold. This reduction in noise led to fewer hits in the TMT experiment, which only had 14
366 proteins that were 2-fold enriched in the tubule samples (Fig. **2c**, Supporting Information
367 Dataset **S3**).
368
369 We consolidated the results of all three experiments into one list of high-confidence tubule
370 proteins by selecting only the proteins that were at least 2-fold tubule-enriched in at least two
371 out of three of the membrane purifications. There were only six such proteins, which are listed in
372 Table **2**. Four of these six proteins are previously-known tubule proteins: the two bait proteins
373 RBMP1 and RBMP2, the carbonic anhydrase CAH3 (Sinetova *et al.*, 2012), and MITH1
374 (Hennacy *et al.*, 2024).
375
376 While these four proteins do not represent all previously-known tubule-localized proteins, the
377 nature of our experiment is such that we measured protein enrichment relative to the rest of the
378 thylakoid membranes, so our method is less sensitive to proteins that localize to both the
379 tubules and thylakoids. Many tubule-enriched proteins, such as PSAH, TEF14, and HCF136,
380 are observed in the tubules but are also present in the thylakoids (Mackinder, 2017; Wang *et al.*,
381 2023), while others, like CAS1, re-localize from throughout the chloroplast to the tubules in a
382 condition-dependent manner (Wang *et al.*, 2016). For such proteins, we expect that some

383 protein may still be present in the thylakoids under our experimental conditions, decreasing their
384 tubule enrichment factors. Thus, Table **2** does not represent all proteins present in the tubules,
385 only those which are most highly enriched relative to their abundance in the thylakoids in our
386 assay.
387
388 Importantly, our results are consistent with the enrichment of proteins based on membrane
389 proximity rather than direct protein-protein interaction, as we were able to identify proteins not
390 seen in traditional detergent-based affinity purification. Neither MITH1 nor CAH3 co-
391 immunoprecipitated with RBMP1 or RBMP2 in a detergent-based affinity purification
392 (Supporting Information Dataset **S4**), yet both are enriched in our tubule samples (Fig. **2**, Table
393 **2**). The presence of CAH3, a pyrenoid tubule-enriched luminal protein with no predicted
394 transmembrane domains (Sinetova *et al.*, 2012), also suggests that we are able to capture
395 proteins within the membrane lumen. Furthermore, RBMP1 and RBMP2 did not co-precipitate in
396 detergent-based affinity purification (Fig. **1h**, Supporting Information Dataset **S4**), whereas they
397 did co-precipitate in our first and third membrane purifications (Table **2**).
398
399 Taken together, these results indicate that our protocol is able to isolate and identify tubule
400 membrane-enriched proteins that are not captured by traditional affinity purification approaches.
401 These observations gave us confidence in the likelihood that the other two proteins in our top
402 hits were also tubule-localized. These proteins were Low-CO_2-induced 16, also known as Early
403 Light-Induced 4 (LCI16/ELI4; Cre02.g143550) and Cre10.g452250, which we named Pyrenoid
404 Membrane–Enriched 1 (PME1). Given these proteins' presence in our tubule proteome and
405 their relative lack of characterization, we sought to validate their tubule localization and
406 determine if they impact pyrenoid tubule biogenesis.
407
408 **Fluorescently-tagged LCI16 localizes to the pyrenoid-traversing membranes**
409 We created constructs to express each novel tubule candidate gene tagged with a Venus
410 fluorophore and transformed each construct into wild-type cells (CMJ030). Multiple PME1-
411 Venus-3×FLAG constructs, using both the native promoter and the highly-expressing PSAD
412 promoter, consistently failed to yield detectable levels of Venus fluorescence, even among
413 antibiotic-resistant colonies that appeared to have been successfully transformed. Antibodies
414 raised against PME1 also failed to produce a PME1-specific signal, preventing us from using
415 them effectively to localize PME1. These challenges may be related to PME1's low native

416 abundance (Fig. **6**, Supporting Information Fig. **S2a**). Thus, we focused our efforts on
417 characterizing LCI16-Venus-3×FLAG transformants, which yielded detectable fluorescence.
418
419 We observed via fluorescence microscopy that LCI16-Venus-3×FLAG localizes to the center of
420 the pyrenoid (Fig. **3a**). Its localization pattern was concentrated near the center of the pyrenoid,
421 more similar to the pattern of known tubule proteins RBMP1 and RBMP2 (Fig. **1d,e**) than to the
422 pattern of matrix-localized proteins such as Rubisco or EPYC1 (Meyer *et al.*, 2020b). We
423 attempted to determine the localization of LCI16 more precisely by co-localizing it with RBMP2-
424 Venus using an antibody raised against LCI16. However, the α-LCI16 antibody stained the
425 entire chloroplast, including the pyrenoid (Supporting Information Fig. **S3b**). This could indicate
426 that LCI16 localizes to the entire chloroplast, or that the antibody is not specific to LCI16. To
427 distinguish between these possibilities, we stained a mutant lacking LCI16 expression with the
428 α-LCI16 antibody and compared it to α-LCI16 staining in wild-type cells. In the *lci16* mutant
429 strain, the non-pyrenoidal signal remained, but the pyrenoid signal was no longer observed
430 (Supporting Information Fig. **S3e**), indicating that the non-pyrenoidal signal in wild-type cells
431 was likely non-specific. Futhermore, the loss of α-LCI16 pyrenoid staining in the *lci16* mutant is
432 consistent with a pyrenoid localization for LCI16, as observed in the LCI16-Venus-3×FLAG
433 strain. Based on LCI16's enrichment in our tubule membrane proteome and the localization
434 pattern observed for LCI16-Venus-3×FLAG, we conclude that LCI16 localizes to pyrenoid-
435 traversing membranes.
436
437 **LCI16 physically interacts with RBMP2 and PME1**
438 To further investigate the role of LCI16 in the tubule membranes, we performed a traditional
439 detergent-based affinity purification using LCI16-Venus-3×FLAG as bait to identify its protein
440 interactors (Fig. **3b**, Supporting Information Dataset **S5**). In this experiment, the top two
441 interactors of LCI16 were PME1 and RBMP2. This indicates that these three proteins physically
442 interact, directly or indirectly, providing additional support for PME1's tubule localization.
443
444 Our previous detergent-based RBMP2-Venus-3×FLAG affinity purification did not identify LCI16
445 or PME1 as highly enriched (Supporting Information Dataset **S4**). However, previously-
446 published proteomic data from diurnally-grown cells (Strenkert *et al.*, 2019) suggest that RBMP2
447 is more abundant than LCI16 or PME1 (Supporting Information Fig. **S2**), raising the possibility
448 that a large proportion of LCI16 and PME1 may be bound to RBMP2 even while the majority of
449 RBMP2 is not bound to LCI16 or PME1.

450

451 **Transmission electron microscopy (TEM) of insertional mutants in LCI16 and PME1**
452 **indicates that neither protein is required for normal tubule morphology**
453 To assess whether LCI16 and PME1 play structural roles in pyrenoid tubule biogenesis, we
454 examined pyrenoid morphology in mutant strains lacking expression of each protein using
455 transmission electron microscopy (TEM). We obtained three mutant alleles for both LCI16 and
456 PME1, with four mutants coming from the CLiP collection (Li *et al.*, 2019) and two mutants
457 coming from the more recently-developed CLiP2 collection (Lunardon *et al.*, 2024). We
458 confirmed the insertion sites in all six mutants by PCR (Supporting Information Fig. **S4**) and
459 examined all mutants by electron microscopy.
460
461 Unlike *mith1* and *saga1* mutants, which have the most severe tubule-related defects observed
462 in *C. reinhardtii* to date—with most Rubisco condensates entirely lacking tubules (Hennacy *et*
463 *al.*, 2024)—the *lci16* and *pme1* mutants examined by TEM showed wild-type pyrenoid
464 morphology. We regularly observed only one pyrenoid per cell, and we could observe central
465 reticulated regions (Fig. **4b,e,h**) and peripheral cylindrical tubules with minitubules (Fig. **4c,f,i**,
466 Supporting Information Fig. **S5**) that were indistinguishable from those in wild-type cells. These
467 results indicate that LCI16 and PME1 are not required for normal tubule morphology under our
468 culture conditions and suggest that they function in processes unrelated to tubule biogenesis.
469
470 ***lci16* and *pme1* mutants have normal growth under CCM-requiring conditions**
471 We further investigated the role of LCI16 and PME1 in CCM function by performing spot tests
472 on the *lci16* and *pme1* insertional mutants under increasingly CO_2-limiting growth conditions
473 (Fig. **5**). We compared the growth of mutants to the growth of their respective wild-type
474 background strains, as well as to the growth of *saga1* and *mith1* mutants, which are known to
475 have CCM defects (Itakura *et al.*, 2019; Hennacy *et al.*, 2024).
476
477 All strains grew as well as wild-type under high CO_2 (Fig. **5a**). As expected, the *saga1* and *mith1*
478 mutants suffered increasingly severe growth defects as the CO_2 level decreased and the light
479 intensity increased (Fig. **5b-e**). However, the *lci16* and *pme1* mutants grew as well as their
480 respective wild-type strains under all conditions tested, with the exception of one *pme1* mutant,
481 *pme1-1*, which had a mild growth defect under very low CO_2. Given that two of the three *pme1*
482 mutants displayed no CCM growth defect, it is most likely that a second, off-site mutation in

483 *pme1-1* is responsible for its growth defect. Together, these results suggest that neither LCI16
484 nor PME1 is required for proper CCM function under the conditions tested.
485
486 **Proteomes of the *lci16* and *pme1* mutants are similar to those of known CCM mutants**
487 Since the *lci16* and *pme1* mutants had no defect in their tubules and no visible growth defect
488 under the conditions tested, we sought to determine whether they impact the proteome. We
489 used mass spectrometry to determine whole-cell proteomes of two alleles each of *lci16* and
490 *pme1*; both of their wild-type background strains; and four mutants with known CCM defects—
491 *cia5*, *epyc1*, *mith1*, and *saga1* (Fig. **6**, Supporting Information Datasets **S6-7**). Many known
492 CCM-related proteins showed similar patterns of regulation across all the known CCM
493 mutants—the putative bicarbonate transporter BST2 was upregulated, while the bicarbonate
494 transporters HLA3 and LCIA and the carbonic anhydrases CAH1, CAH2, CAH5, and LCID were
495 downregulated.
496
497 The *pme1* and *lci16* mutants had similar proteomic profiles to the known CCM mutants,
498 exhibiting upregulation of BST2 and downregulation of HLA3, LCIA, and CAH3. This similarity in
499 proteomic profile is not due to a general growth defect, as the proteomic changes were
500 observed in alleles of *pme1* and *lci16* that have wild-type-like growth under all conditions tested.
501 Considering that disrupting genes in the same pathway typically leads to similar perturbations to
502 the proteome (Kafri *et al.*, 2023), we interpret the similarity of *pme1* and *lci16* proteomes to
503 those of known CCM mutants as an indication that PME1 and LCI16 share a function with CIA5,
504 EPYC1, MITH1, and SAGA1 as perceived by cellular regulatory networks.
505

506 # Discussion

507 **Benefits and limitations of the membrane affinity purification protocol**
508 In this study, we enriched pyrenoid-traversing membrane fragments from *C. reinhardtii* and
509 identified their associated proteins. From this dataset, we further characterized two novel tubule
510 protein candidates, LCI16 and PME1.
511
512 Our membrane affinity purification approach overcame the challenge that pyrenoid tubules are
513 contiguous with—and vastly less abundant than—the thylakoid membranes, impeding their
514 isolation by traditional membrane fractionation methods (Bailyes *et al.*, 1997; Avila *et al.*, 2015).
515 Our protocol overcame this challenge by enriching specific membrane subdomains based on
516 the presence of a known resident protein, allowing us to identify novel protein components of

517 the chosen membrane starting with only the identity of two of its protein components. The
518 limitations of our implementation included low-number sampling noise due to the label-free
519 quantification used in the first two experiments, which limited our ability to detect lower-
520 abundance proteins, and changes to the protocol over the three iterations, which we think
521 contributed to variability in hits between the experiments. With further improvements, we believe
522 our approach could be applied to determine the protein composition of other membrane
523 domains on a sub-organellar level.
524
525 **Possible functions for the novel tubule components LCI16 and PME1**
526 One of the proteins identified by our protocol is Low-CO_2-Induced 16 (LCI16), also known as
527 Early Light-Induced 4 (ELI4). LCI16 has a light-harvesting complex (LHC)-like domain
528 homologous to those found in the stress-related LHCs (LHCSR) and Early Light-Induced Protein
529 (ELIP) families, which are characterized by a 3-helix chlorophyll-binding domain (Rochaix &
530 Bassi, 2019; Levin & Schuster, 2023). These proteins are present across plant and algal
531 species; are often induced by dark-to-light transitions, high light, and/or other abiotic stresses;
532 and typically function in photoprotection via non-photochemical quenching (NPQ), as well as
533 assembly of new photosystems or repair of damaged photosystems (Montané & Kloppstech,
534 2000; Rochaix & Bassi, 2019; Levin & Schuster, 2023). Unlike the ELIPs, however, LCI16
535 retains relatively high mRNA levels throughout the night, and its expression profile is much more
536 similar to that of RBMP2 than any of the other ELIPs (Supporting Information Fig. **S2**). Given its
537 transcriptional similarity to and physical interaction with RBMP2, it is likely that LCI16 plays a
538 more pyrenoid-specific role than other ELIP proteins. Further, the fact that LCI16 is not required
539 for growth in the light indicates that any light energy absorbed by chlorophyll in the tubules must
540 be used or dissipated by proteins other than LCI16. These could be other, redundant light stress
541 proteins, or they could be tubule-localized photosystem components (Mackinder, 2017; Wang *et*
542 *al.*, 2023), which may pump protons into the tubule lumen to drive the conversion of HCO_3^- to
543 CO_2 by CAH3. Further work on LCI16 and other tubule-localized light-responsive proteins will be
544 required to determine if the tubules perform any such light-dependent functions beyond serving
545 as the interface between the Rubisco matrix and the conversion of CO_2 by CAH3.
546
547 The other novel tubule protein we identified and characterized, PME1, co-precipitates with
548 LCI16 (Fig. **3b**). While we could not identify any homologs of PME1, it has several non-
549 canonical PRICHEXTENSN-like motifs reminiscent of similar proline-rich domains previously
550 described in proteins associated with plant cell wall stability (Showalter *et al.*, 2010; Goodstein

551 *et al.*, 2012; Guo *et al.*, 2014; Craig *et al.*, 2023). The C-terminus of PME1 is predicted by
552 Alphafold 3 (Abramson *et al.*, 2024) to fold into a series of beta sheets followed by a long
553 amphipathic helix which may oligomerize as a coiled coil homo-trimer (Supporting Information
554 Fig. **S6a-b**). Amphipathic helices and coiled coils are common oligomerization domains
555 (Truebestein & Leonard, 2016), but they are also common among several families of
556 membrane-binding and -shaping proteins, such as BAR domain proteins (Gallop *et al.*, 2006;
557 Jao *et al.*, 2010) and reticulons (Brooks *et al.*, 2021), suggesting a potential mechanism for
558 membrane binding in the C-terminal domain of PME1.
559
560 Our whole-cell proteome experiments also found that PME1 is highly upregulated in the *cia5*
561 and *mith1* mutants (Fig. **6**). This is unusual considering that most CCM-related proteins are
562 downregulated in these mutants—and because under most conditions, PME1 is expressed at
563 very low, often undetectable, levels (Strenkert *et al.*, 2019; Kafri *et al.*, 2023). These
564 observations raise the possibility that PME1 contributes to CCM regulation, e.g. by promoting
565 expression of CCM-related transporters and carbonic anhydrases in response to inadequate
566 CCM function. Further experiments will be required to determine if PME1 plays such a
567 regulatory role, and under what conditions, if any, it is required for full CCM function.
568
569 Taken together, our results identify LCI16 and PME1 as novel pyrenoid-traversing membrane
570 components, initiate their characterization, and suggest directions for future research into their
571 functions. Our pyrenoid-traversing membrane proteome identifies known components and
572 additional candidates, helping to prioritize proteins for future study. We hope these findings will
573 ultimately contribute toward a mechanistic understanding of the pyrenoid, an organelle with a
574 central role in the global carbon cycle.

Acknowledgments

We would like to thank Saw Kyin and Henry Shwe of the Princeton University Proteomics Core and the Thermo Fisher Scientific Center for Multiplexed Proteomics at Harvard Medical School (https://tcmp.hms.harvard.edu) for advice and help performing mass spectroscopy; John Schreiber and Paul Shao of the Princeton Imaging & Analysis Center for advice and technical support for electron microscopy; Michelle Warren-Williams for media preparation and propagating strains; Victoria L. Crans and Micah Burton for sharing reagents, experimental assistance, and feedback on the manuscript; Ned Wingreen, Fred Hughson, and members of the Jonikas laboratory for project feedback and helpful conversations; and Marie Bao, as part of Life Science Editors, for help with editing the manuscript. The authors acknowledge the use of the Imaging and Analysis Center (IAC) operated by the Princeton Materials Institute at Princeton University, which is supported in part by the Princeton Center for Complex Materials (PCCM), a National Science Foundation (NSF) Materials Research Science and Engineering Center (MRSEC; DMR-2011750). Research reported in this paper was supported by the Howard Hughes Medical Institute, Bill and Melinda Gates Foundation and United Kingdom Foreign, Commonwealth & Development Office grant INV-054558, National Science Foundation grants MCB-2410354 and MCB-1914989, and NIGMS of the National Institutes of Health grants 1R01GM140032-01 and T32GM007388. The content is solely the responsibility of the authors and does not necessarily represent the official views of the National Institutes of Health.

Competing Interests

None declared.

Author contributions

EF and MCJ conceived of and planned the project. EF, ERC, KD, and SLE performed the membrane purification experiments and EF analyzed the mass spectrometry data. EF performed the TEM imaging, growth assays, and sample preparation for whole cell proteomics. LW performed detergent-based affinity purifications; LW and AG performed fluorescence microscopy. AL, WP, and CP generated and identified the CLiP2 mutants. EF and MCJ wrote the manuscript.

Data Availability

The data that supports the findings of this study are available in Supporting Information Datasets **S1-7** included with this article.

References

Abramson J, Adler J, Dunger J, Evans R, Green T, Pritzel A, Ronneberger O, Willmore L, Ballard AJ, Bambrick J, *et al.* 2024. Accurate structure prediction of biomolecular interactions with AlphaFold 3. *Nature* **630**: 493–500.

Adler L, Lau CS, Shaikh KM, van Maldegem KA, Payne-Dwyer AL, Lefoulon C, Girr P, Atkinson N, Barrett J, Emrich-Mills TZ, *et al.* 2024. Bestrophin-like protein 4 is involved in photosynthetic acclimation to light fluctuations in Chlamydomonas. *Plant Physiology* **196**: 2374–2394.

Avila JR, Lee JS, Torii KU. **2015**. Co-Immunoprecipitation of Membrane-Bound Receptors. *The Arabidopsis Book / American Society of Plant Biologists* **13**: e0180.

Bailyes EM, Navé BT, Soos MA, Orr SR, Hayward AC, Siddle K. **1997**. Insulin receptor/IGF-I receptor hybrids are widely distributed in mammalian tissues: quantification of individual receptor species by selective immunoprecipitation and immunoblotting. *Biochemical Journal* **327**: 209–215.

Barrett J, Girr P, Mackinder LCM. **2021**. Pyrenoids: CO2-fixing phase separated liquid organelles. *Biochimica et Biophysica Acta (BBA) - Molecular Cell Research* **1868**: 118949.

Beardall J, Raven JA. **2020**. Structural and Biochemical Features of Carbon Acquisition in Algae. In: Larkum AWD, Grossman AR, Raven JA, eds. Advances in Photosynthesis and Respiration – Including Bioenergy and Related Processes. Photosynthesis in Algae: Biochemical and Physiological Mechanisms. 141–160.

Behnke J-S, Urner LH. **2023**. Emergence of mass spectrometry detergents for membrane proteomics. *Analytical and Bioanalytical Chemistry* **415**: 3897–3909.

Brooks RL, Mistry CS, Dixon AM. **2021**. Curvature sensing amphipathic helix in the C-terminus of RTNLB13 is conserved in all endoplasmic reticulum shaping reticulons in Arabidopsis thaliana. *Scientific Reports* **11**: 6326.

Caspari OD, Meyer MT, Tolleter D, Wittkopp TM, Cunniffe NJ, Lawson T, Grossman AR, Griffiths H. **2017**. Pyrenoid loss in Chlamydomonas reinhardtii causes limitations in CO2 supply, but not thylakoid operating efficiency. *Journal of Experimental Botany* **68**: 3903–3913.

Chen WW, Freinkman E, Wang T, Birsoy K, Sabatini DM. **2016**. Absolute Quantification of Matrix Metabolites Reveals the Dynamics of Mitochondrial Metabolism. *Cell* **166**: 1324-1337.e11.

Chen C, Sidransky E, Chen Y. **2022**. Lyso-IP: Uncovering Pathogenic Mechanisms of Lysosomal Dysfunction. *Biomolecules* **12**: 616.

Craig RJ, Gallaher SD, Shu S, Salomé PA, Jenkins JW, Blaby-Haas CE, Purvine SO, O'Donnell S, Barry K, Grimwood J, *et al.* 2023. The Chlamydomonas Genome Project, version 6: Reference assemblies for mating-type plus and minus strains reveal extensive structural mutation in the laboratory. *The Plant Cell* **35**: 644–672.

Ellis RJ. **1979**. The most abundant protein in the world. *Trends in Biochemical Sciences* **4**: 241–244.

Engel BD, Schaffer M, Cuellar LK, Villa E, Pitzko JM, Baumeister W. **2015**. Chlamydomonas chloroplast revealed by in situ cryo-electron tomography. *eLife* **4**.

Fei C, Wilson AT, Mangan NM, Wingreen NS, Jonikas MC. **2022**. Modelling the pyrenoid-based CO2-concentrating mechanism provides insights into its operating principles and a roadmap for its engineering into crops. *Nature Plants* **8**: 583–595.

Field CB, Behrenfeld MJ, Randerson JT, Falkowski P. **1998**. Primary Production of the Biosphere: Integrating Terrestrial and Oceanic Components. *Science* **281**: 237–240.

Flamholz AI, Prywes N, Moran U, Davidi D, Bar-On YM, Oltrogge LM, Alves R, Savage D, Milo R. **2019**. Revisiting Trade-offs between Rubisco Kinetic Parameters. *Biochemistry* **58**: 3365–3376.

Freeman Rosenzweig ES, Xu B, Cuellar LK, Martinez-Sanchez A, Schaffer M, Strauss M, Cartwright HN, Ronceray P, Plitzko JM, Förster F, *et al.* 2017. The Eukaryotic CO2-Concentrating Organelle Is Liquid-like and Exhibits Dynamic Reorganization. *Cell* **171**: 148-162.e19.

Gallop JL, Jao CC, Kent HM, Butler PJG, Evans PR, Langen R, McMahon HT. **2006**. Mechanism of endophilin N-BAR domain-mediated membrane curvature. *The EMBO journal* **25**: 2898–2910.

Goodenough UW. **1970**. Chloroplast Division and Pyrenoid Formation in Chlamydomonas Reinhardi. *Journal of Phycology* **6**: 1–6.

Goodenough UW, Levine RP. **1970**. CHLOROPLAST STRUCTURE AND FUNCTION IN ac-20, A MUTANT STRAIN OF CHLAMYDOMONAS REINHARDI : III. Chloroplast Ribosomes and Membrane Organization. *Journal of Cell Biology* **44**: 547–562.

Goodstein DM, Shu S, Howson R, Neupane R, Hayes RD, Fazo J, Mitros T, Dirks W, Hellsten U, Putnam N, *et al.* 2012. Phytozome: a comparative platform for green plant genomics. *Nucleic Acids Research* **40**: D1178–D1186.

Guo L, Chen Y, Ye N, Dai X, Yang W, Yin T. **2014**. Differential retention and expansion of the ancestral genes associated with the paleopolyploidies in modern rosid plants, as revealed by analysis of the extensins super-gene family. *BMC Genomics* **15**: 612.

Hatch MD. **1987**. C4 photosynthesis: a unique blend of modified biochemistry, anatomy and ultrastructure. *Biochimica et Biophysica Acta (BBA) - Reviews on Bioenergetics* **895**: 81–106.

He S, Chou H-T, Matthies D, Wunder T, Meyer MT, Atkinson N, Martinez-Sanchez A, Jeffrey PD, Port SA, Patena W, *et al.* 2020. The structural basis of Rubisco phase separation in the pyrenoid. *Nature Plants* **6**: 1480–1490.

He S, Crans VL, Jonikas MC. **2023**. The pyrenoid: the eukaryotic CO2-concentrating organelle. *The Plant Cell* **35**: 3236–3259.

Hennacy JH, Atkinson N, Kayser-Browne A, Ergun SL, Franklin E, Wang L, Kafri M, Fauser F, Vilarrasa-Blasi J, Jinkerson RE, *et al.* 2024. Biogenesis, engineering and function of membranes in the CO2-fixing pyrenoid. : 2024.08.08.603944.

Itakura AK, Chan KX, Atkinson N, Pallesen L, Wang L, Reeves G, Patena W, Caspari O, Roth R, Goodenough U, *et al.* 2019. A Rubisco-binding protein is required for normal pyrenoid number and starch sheath morphology in Chlamydomonas reinhardtii. *Proceedings of the National Academy of Sciences* **116**: 18445–18454.

691 **Jao CC, Hegde BG, Gallop JL, Hegde PB, McMahon HT, Haworth IS, Langen R**. **2010**.
692 Roles of amphipathic helices and the bin/amphiphysin/rvs (BAR) domain of endophilin in
693 membrane curvature generation. *The Journal of Biological Chemistry* **285**: 20164–20170.

694 **Kafri M, Patena W, Martin L, Wang L, Gomer G, Ergun SL, Sirkejyan AK, Goh A, Wilson**
695 **AT, Gavrilenko SE, *et al.* 2023**. Systematic identification and characterization of genes in the
696 regulation and biogenesis of photosynthetic machinery. *Cell* **186**: 5638-5655.e25.

697 **Karlsson J, Clarke AK, Chen ZY, Hugghins SY, Park YI, Husic HD, Moroney JV,**
698 **Samuelsson G**. **1998**. A novel alpha-type carbonic anhydrase associated with the thylakoid
699 membrane in Chlamydomonas reinhardtii is required for growth at ambient CO2. *The EMBO*
700 *Journal* **17**: 1208–1216.

701 **Kyte J, Doolittle RF**. **1982**. A simple method for displaying the hydropathic character of a
702 protein. *Journal of Molecular Biology* **157**: 105–132.

703 **Lau CS, Dowle A, Thomas GH, Girr P, Mackinder LCM**. **2023**. A phase-separated CO2-fixing
704 pyrenoid proteome determined by TurboID in Chlamydomonas reinhardtii. *The Plant Cell* **35**:
705 3260–3279.

706 **Levin G, Schuster G**. **2023**. LHC-like Proteins: The Guardians of Photosynthesis. *International*
707 *Journal of Molecular Sciences* **24**: 2503.

708 **Li X, Patena W, Fauser F, Jinkerson RE, Saroussi S, Meyer MT, Ivanova N, Robertson JM,**
709 **Yue R, Zhang R, *et al.* 2019**. A genome-wide algal mutant library and functional screen
710 identifies genes required for eukaryotic photosynthesis. *Nature Genetics* **51**: 627–635.

711 **Li J, Van Vranken JG, Pontano Vaites L, Schweppe DK, Huttlin EL, Etienne C,**
712 **Nandhikonda P, Viner R, Robitaille AM, Thompson AH, *et al.* 2020**. TMTpro reagents: a set
713 of isobaric labeling mass tags enables simultaneous proteome-wide measurements across 16
714 samples. *Nature Methods* **17**: 399–404.

715 **Lunardon A, Patena W, Pacini C, Warren-Williams M, Zubak Y, Laudon M, Silflow C,**
716 **Lefebvre P, Jonikas M**. **2024**. The Chlamydomonas reinhardtii CLiP2 mutant collection
717 expands genome coverage with high-confidence disrupting alleles. : 2024.12.16.626622.

718 **Lüttge U**. **2004**. Ecophysiology of Crassulacean Acid Metabolism (CAM). *Annals of Botany* **93**:
719 629–652.

720 **Ma Y, Pollock SV, Xiao Y, Cunnusamy K, Moroney JV**. **2011**. Identification of a Novel Gene,
721 CIA6, Required for Normal Pyrenoid Formation in Chlamydomonas reinhardtii. *Plant Physiology*
722 **156**: 884–896.

723 **Mackinder L**. **2017**. A Spatial Interactome Reveals the Protein Organization of the Algal CO2
724 Concentrating Mechanism. Mackinder et al. *Cell* **171**: 133-147.e14.

725 **Mackinder LCM, Meyer MT, Mettler-Altmann T, Chen VK, Mitchell MC, Caspari O,**
726 **Rosenzweig ESF, Pallesen L, Reeves G, Itakura A, *et al.* 2016**. A repeat protein links
727 Rubisco to form the eukaryotic carbon-concentrating organelle. *Proceedings of the National*
728 *Academy of Sciences* **113**: 5958–5963.

729 **McAlister GC, Huttlin EL, Haas W, Ting L, Jedrychowski MP, Rogers JC, Kuhn K, Pike I,**
730 **Grothe RA, Blethrow JD, *et al.* 2012**. Increasing the Multiplexing Capacity of TMTs Using
731 Reporter Ion Isotopologues with Isobaric Masses. *Analytical Chemistry* **84**: 7469–7478.

732 **Meyer MT, Goudet MMM, Griffiths H**. **2020a**. The Algal Pyrenoid. In: Larkum AWD, Grossman
733 AR, Raven JA, eds. Advances in Photosynthesis and Respiration – Including Bioenergy and
734 Related Processes. Photosynthesis in Algae: Biochemical and Physiological Mechanisms. 179–
735 203.

736 **Meyer MT, Itakura AK, Patena W, Wang L, He S, Emrich-Mills T, Lau CS, Yates G,**
737 **Mackinder LCM, Jonikas MC**. **2020b**. Assembly of the algal CO2-fixing organelle, the
738 pyrenoid, is guided by a Rubisco-binding motif. *Science Advances* **6**: eabd2408.

739 **Meyer K, Selbach M**. **2015**. Quantitative affinity purification mass spectrometry: a versatile
740 technology to study protein–protein interactions. *Frontiers in Genetics* **6**: 237.

741 **Montané M-H, Kloppstech K**. **2000**. The family of light-harvesting-related proteins (LHCs,
742 ELIPs, HLIPs): was the harvesting of light their primary function? *Gene* **258**: 1–8.

743 **Morris JH, Knudsen GM, Verschueren E, Johnson JR, Cimermancic P, Greninger AL,**
744 **Pico AR**. **2014**. Affinity purification–mass spectrometry and network analysis to understand
745 protein-protein interactions. *Nature protocols* **9**: 2539–2554.

Mukherjee A, Lau CS, Walker CE, Rai AK, Prejean CI, Yates G, Emrich-Mills T, Lemoine SG, Vinyard DJ, Mackinder LCM, *et al.* 2019. Thylakoid localized bestrophin-like proteins are essential for the CO2 concentrating mechanism of Chlamydomonas reinhardtii. *Proceedings of the National Academy of Sciences* **116**: 16915–16920.

O'Connell JD, Paulo JA, O'Brien JJ, Gygi SP. **2018**. Proteome-Wide Evaluation of Two Common Protein Quantification Methods. *Journal of Proteome Research* **17**: 1934–1942.

Raven JA. **1997**. CO2-concentrating mechanisms: a direct role for thylakoid lumen acidification? *Plant, Cell & Environment* **20**: 147–154.

Raven JA, Beardall J, Sánchez-Baracaldo P. **2017**. The possible evolution and future of CO2-concentrating mechanisms. *Journal of Experimental Botany* **68**: 3701–3716.

Rawat M, Henk MC, Lavigne LL, Moroney JV. **1996**. Chlamydomonas reinhardtii mutants without ribulose-1,5-bisphosphate carboxylase-oxygenase lack a detectable pyrenoid. *Planta* **198**: 263–270.

Rochaix J-D, Bassi R. **2019**. LHC-like proteins involved in stress responses and biogenesis/repair of the photosynthetic apparatus. *Biochemical Journal* **476**: 581–593.

Sage RF, Sage TL, Kocacinar F. **2012**. Photorespiration and the evolution of C4 photosynthesis. *Annu. Rev. Plant Biol.* **63**: 19–47.

Schindelin J, Arganda-Carreras I, Frise E, Kaynig V, Longair M, Pietzsch T, Preibisch S, Rueden C, Saalfeld S, Schmid B, *et al.* 2012. Fiji: an open-source platform for biological-image analysis. *Nature Methods* **9**: 676–682.

Showalter AM, Keppler B, Lichtenberg J, Gu D, Welch LR. **2010**. A Bioinformatics Approach to the Identification, Classification, and Analysis of Hydroxyproline-Rich Glycoproteins. *Plant Physiology* **153**: 485–513.

Sinetova MA, Kupriyanova EV, Markelova AG, Allakhverdiev SI, Pronina NA. **2012**. Identification and functional role of the carbonic anhydrase Cah3 in thylakoid membranes of pyrenoid of Chlamydomonas reinhardtii. *Biochimica et biophysica acta* **1817**: 1248.

Strenkert D, Schmollinger S, Gallaher SD, Salomé PA, Purvine SO, Nicora CD, Mettler-Altmann T, Soubeyrand E, Weber APM, Lipton MS, *et al.* 2019. Multiomics resolution of

774 molecular events during a day in the life of Chlamydomonas. *Proceedings of the National*
775 *Academy of Sciences* **116**: 2374–2383.

776 **Ting L, Rad R, Gygi SP, Haas W**. **2011**. MS3 eliminates ratio distortion in isobaric multiplexed
777 quantitative proteomics. *Nature Methods* **8**: 937–940.

778 **Toyokawa C, Yamano T, Fukuzawa H**. **2020**. Pyrenoid Starch Sheath Is Required for LCIB
779 Localization and the CO_2 -Concentrating Mechanism in Green Algae. *Plant Physiology* **182**:
780 1883–1893.

781 **Truebestein L, Leonard TA**. **2016**. Coiled-coils: The long and short of it. *Bioessays* **38**: 903–
782 916.

783 **Wang L, Patena W, Van Baalen KA, Xie Y, Singer ER, Gavrilenko S, Warren-Williams M,**
784 **Han L, Harrigan HR, Hartz LD, *et al.* 2023**. A chloroplast protein atlas reveals punctate
785 structures and spatial organization of biosynthetic pathways. *Cell* **186**: 3499-3518.e14.

786 **Wang Y, Stessman DJ, Spalding MH**. **2015**. The CO2 concentrating mechanism and
787 photosynthetic carbon assimilation in limiting CO2: how Chlamydomonas works against the
788 gradient. *The Plant Journal* **82**: 429–448.

789 **Wang L, Yamano T, Takane S, Niikawa Y, Toyokawa C, Ozawa S, Tokutsu R, Takahashi Y,**
790 **Minagawa J, Kanesaki Y, *et al.* 2016**. Chloroplast-mediated regulation of CO2-concentrating
791 mechanism by Ca2+-binding protein CAS in the green alga Chlamydomonas reinhardtii.
792 *Proceedings of the National Academy of Sciences* **113**: 12586–12591.

793 **Yamano T, Fukuzawa H**. **2016**. Indirect Immunofluorescence Assay in Chlamydomonas
794 reinhardtii. *BIO-PROTOCOL* **6**.

795 **Yao J, Qiu Y, Jia L, Zacks DN**. **2018**. Autophagosome immunoisolation from GFP-LC3B
796 mouse tissue. *Autophagy* **15**: 341–346.

797 **Zhan Y, Marchand CH, Maes A, Mauries A, Sun Y, Dhaliwal JS, Uniacke J, Arragain S,**
798 **Jiang H, Gold ND, *et al.* 2018**. Pyrenoid functions revealed by proteomics in Chlamydomonas
799 reinhardtii. *PLOS ONE* **13**: e0185039.

800 **Zhang R, Patena W, Armbruster U, Gang SS, Blum SR, Jonikas MC**. **2014**. High-Throughput
801 Genotyping of Green Algal Mutants Reveals Random Distribution of Mutagenic Insertion Sites
802 and Endonucleolytic Cleavage of Transforming DNA. *The Plant Cell* **26**: 1398–1409.

803 **Zhang L, Wang X, Peng X, Wei Y, Cao R, Liu Z, Xiong J, Ying X, Chen P, Liang S**. **2007**.
804 Immunoaffinity Purification of Plasma Membrane with Secondary Antibody Superparamagnetic
805 Beads for Proteomic Analysis. *Journal of Proteome Research* **6**: 34–43.

806 **Supporting Information Figure S1.** RBMP1 and RBMP2 localize to different regions of the
807 pyrenoid tubules.
808 **Supporting Information Figure S2.** Comparison of LCI16's and PME1's expression profiles in
809 diurnally-grown cells to the expression profiles of known tubule proteins and ELIP proteins
810 **Supporting Information Figure S3.** LCI16 antibody staining is non-specific but consistent with
811 tubule localization and RBMP2 interaction.
812 **Supporting Information Figure S4.** PCR verification of *lci16* and *pme1* insertional mutants
813 **Supporting Information Figure S5.** Additional TEM pyrenoid images of insertional mutants of
814 *lci16* and *pme1*
815 **Supporting Information Figure S6.** Alphafold3 predicts an amphipathic helix and beta sheet in
816 PME1.
817 **Supporting Information Table S1:** Primers used for PCR verification of *lci16* and *pme1*
818 insertional mutants

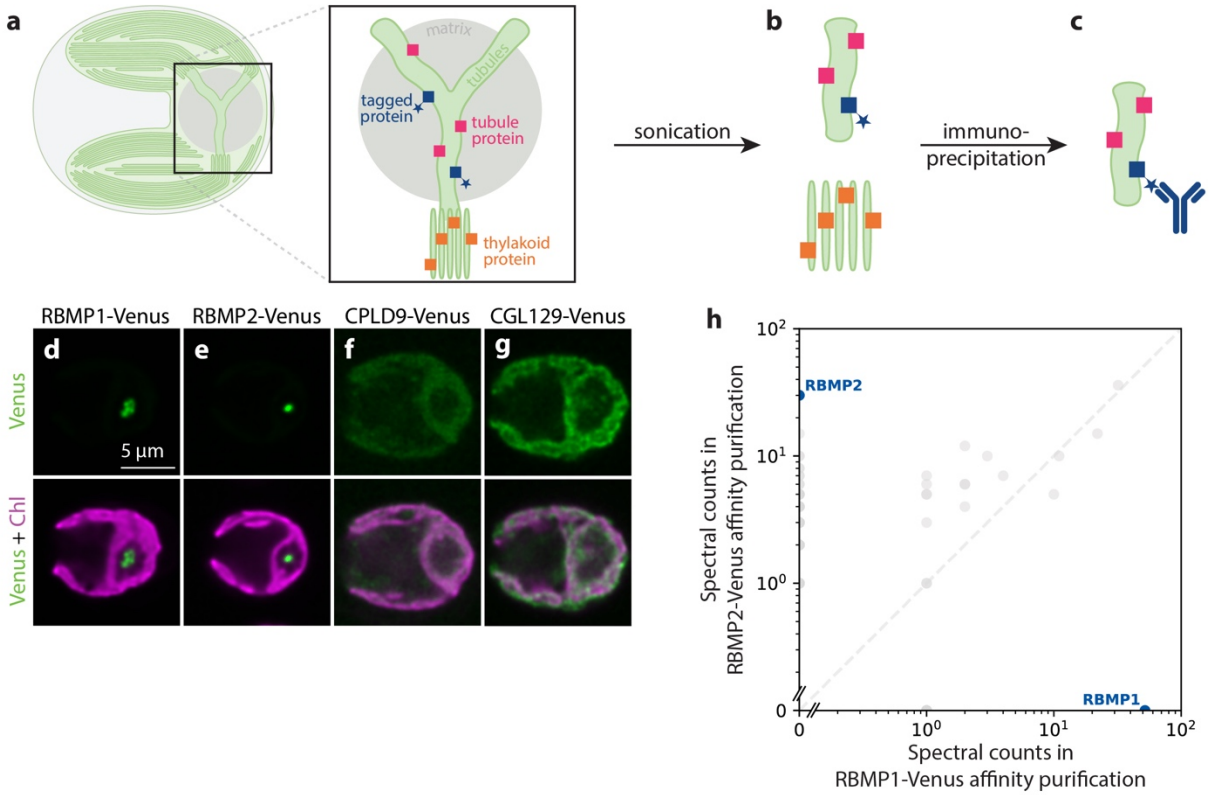

Figure 1: We adapted an affinity purification protocol to isolate intact membranes. **a–c.** Schematic of the membrane affinity purification protocol. **a.** Cartoon representation of a *C. reinhardtii* cell, with the pyrenoid in the base of the cup-shaped chloroplast. Inset: The pyrenoid is traversed by tubule membranes which are contiguous with—but structurally distinct from—the photosynthetic thylakoids. Colored squares represent the proteins localized to the membranes: blue squares with a star represent known tubule proteins tagged with a FLAG tag, pink squares represent all other proteins localized to the tubules, and orange squares represent proteins localized to the thylakoid membranes. **b.** By disrupting cellular membranes using sonication, we created small, intact fragments of pyrenoid tubules (top) and thylakoids (bottom). **c.** Membrane fragments containing tagged proteins were enriched by immunoprecipitation using an anti-FLAG antibody, and their protein composition was determined by mass spectrometry. **d–g.** Confocal fluorescence images showing the localization of the FLAG-tagged proteins used as baits for the membrane affinity purification. Chlorophyll, a proxy for the presence of thylakoid membranes, is shown in magenta. The pyrenoid is visible as a "hole" in the chlorophyll fluorescence at the base of each cell (on the right side of each image). Venus signal is shown in green, representing the localization of the tubule **(d–e)** or thylakoid **(f–g)** bait proteins. **h.** Results of a detergent-based affinity purification show that the tubule bait proteins RBMP1-Venus and RBMP2-Venus do not co-precipitate using traditional affinity purification methods.

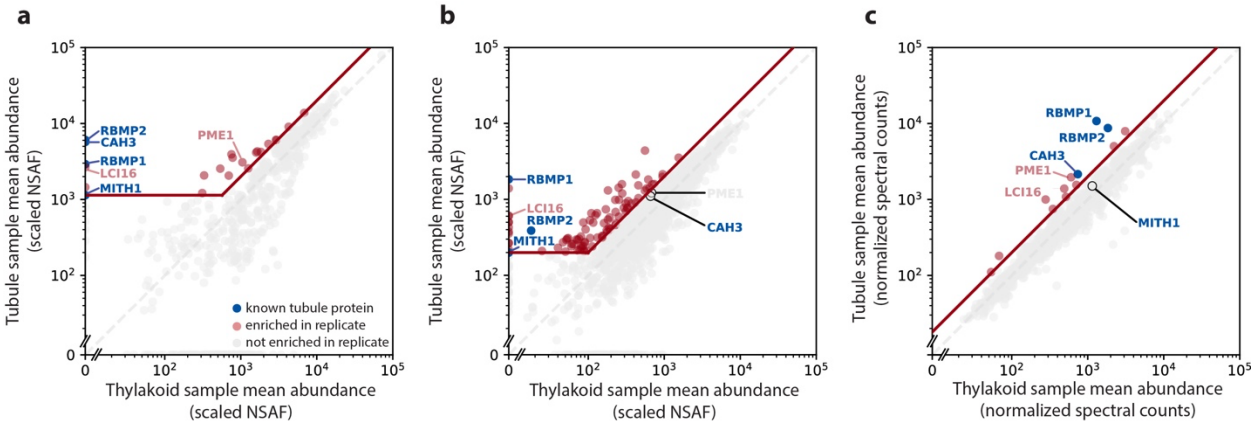

Figure 2: The membrane affinity purification experiment identified both known and novel tubule proteins.

Protein abundances in tubule samples vs. thylakoid samples for the three membrane affinity purification experiments. Blue points represent the known tubule proteins RBMP1, RBMP2, CAH3, and MITH1. The grey dashed lines represent y=x, at which proteins are equally abundant in both the tubule and thylakoid samples. The diagonal red line represents 2-fold enrichment in the tubule samples. The first two experiments **(a–b)** were quantified using label-free quantification, leading to significant noise among lower-abundance proteins. For these experiments, hits (red points) were defined as exceeding 2-fold enrichment in the tubule sample and exceeding a lower abundance threshold (horizontal red line). Proteins in the third membrane affinity purification **(c)** were quantified using tandem mass tagging, leading to better quantification of low-abundance proteins. Thus, only 2-fold enrichment was required to be considered a hit. Proteins that were hits in at least two experiments can be found in Table **2**.

		Experiment 1					Experiment 2					Experiment 3				
Locus	Gene Name	RBMP1	RBMP2	CPLD9	CGL129	fold enrichment	RBMP1	RBMP2	CPLD9	CGL129	fold enrichment	RBMP1	RBMP2	CPLD9	CGL129	fold enrichment
Cre06.g261750	**RBMP1**	5548	281	0	0	INF	3678	0	0	0	INF	19792	1762	1159	1446	8.3
Cre09.g416850	**RBMP2**	3669	8470	0	0	INF	50	727	0	36	21.9	3429	13989	1818	1860	4.7
Cre02.g143550	LCI16	3312	2012	0	0	INF	908	312	0	0	INF	2066	710	478	504	2.8
Cre09.g415700	**CAH3**	5985	5454	0	0	INF	1642	565	549	772	1.7	2955	1346	702	777	2.9
Cre06.g259100	**MITH1**	704	1569	0	0	INF	0	399	0	0	INF	1640	1370	1173	1118	1.3
Cre10.g452250	PME1	1454	4711	1196	906	2.9	798	1646	801	563	1.8	1677	2240	651	555	3.2

Table 2. Proteins enriched in at least two membrane affinity purification experiments

Spectral counts in each affinity purification sample for the proteins identified as enriched in at least two out of the three membrane affinity purification experiments. These values are scaled normalized spectral abundance factor values for experiments 1 and 2, which were quantified using label-free quantification; and normalized spectral counts for experiment 3, which was quantified using tandem-mass-tagging. The names of previously-known tubule proteins are bolded.

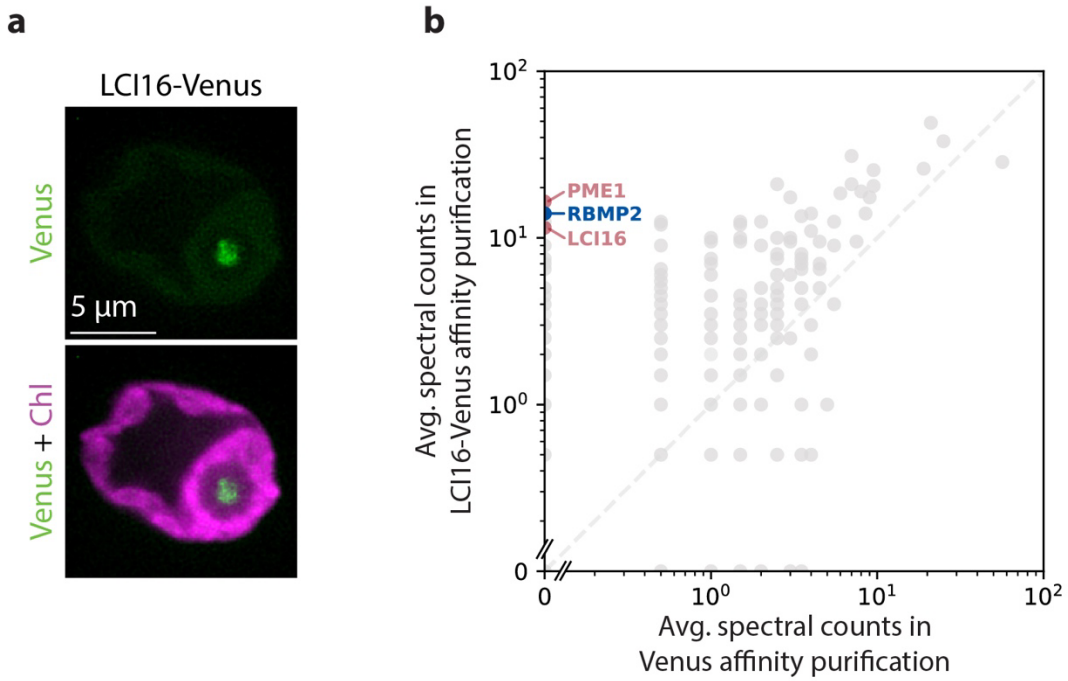

Figure 3: LCI16-Venus localizes to the pyrenoid tubules and co-precipitates RBMP2 and PME1.

a. Confocal images showing the localization of LCI16-Venus in the pyrenoid tubules. Green represents LCI16-Venus signal and magenta represents chlorophyll. **b**. Average spectral counts for a detergent-based affinity purification of LCI16-Venus compared to a control affinity purification of Venus alone. The blue point represents the known tubule protein RBMP2, while the red points represent the novel tubule components LCI16 and PME1.

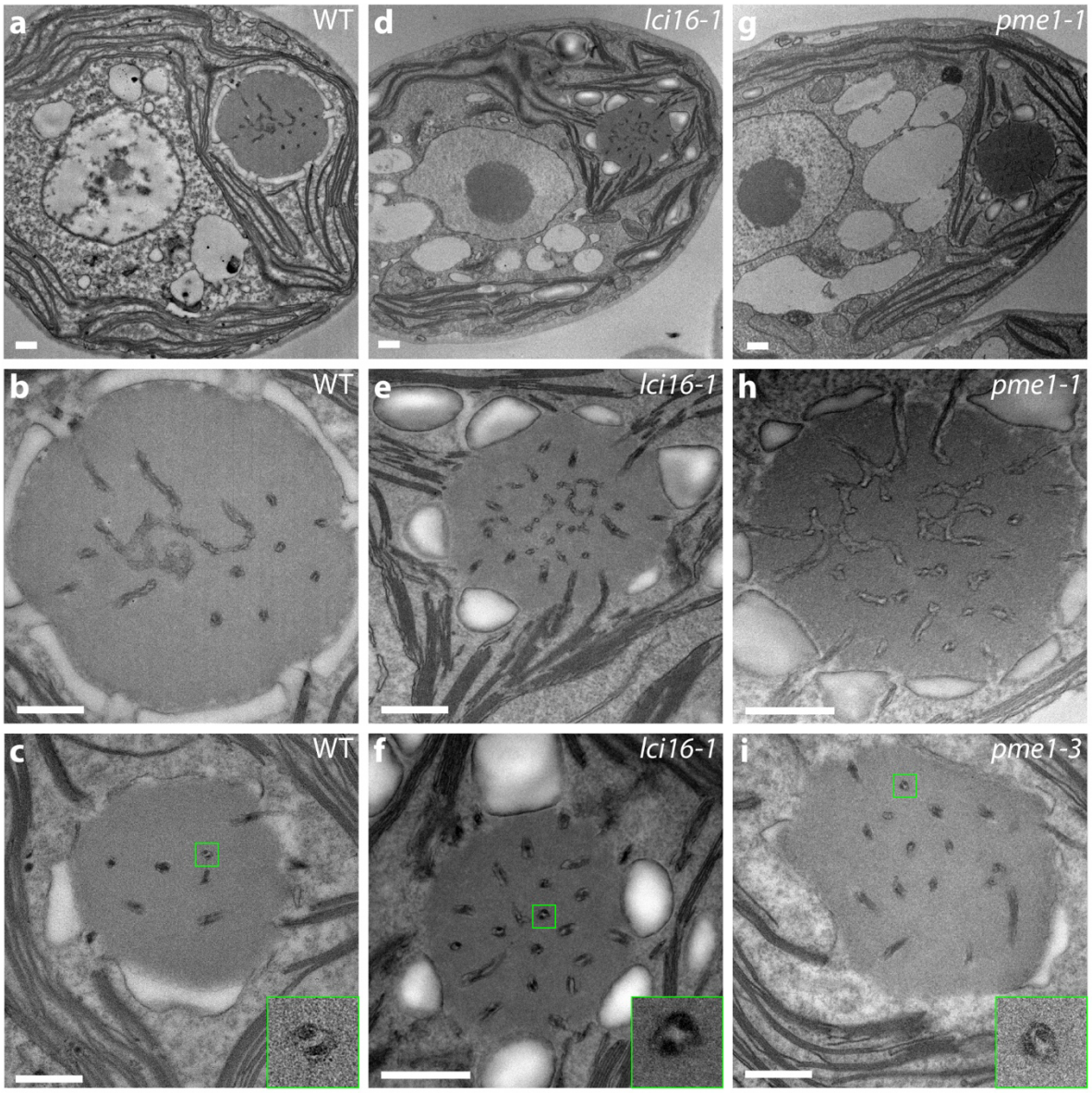

Figure 4: Transmission electron microscopy indicates normal pyrenoid morphology in insertional mutants of *lci16* and *pme1*.

Electron micrographs of wild type **(a–c)**, *lci16* **(d–f)**, and *pme1* **(g–i)** cells. Images of central slices of whole cells **(a,d,g)** show the single pyrenoid in its stereotyped location at the base of the cup-shaped chloroplast. Higher-magnification images of the pyrenoids **(b–c, e–f, h–i)** show tubules in all of the pyrenoids, including both the central reticulated region, characterized by three-way membrane junctions **(b,e,h)**, and the peripheral, minitubule-containing tubules **(c,f,i)**. 4× insets in **(c,f,i)** show individual tubules with visible minitubules. Pyrenoids in **(b,e,h)** represent the same cells as shown in **(a,d,g)**. Scale bars 500 nm.

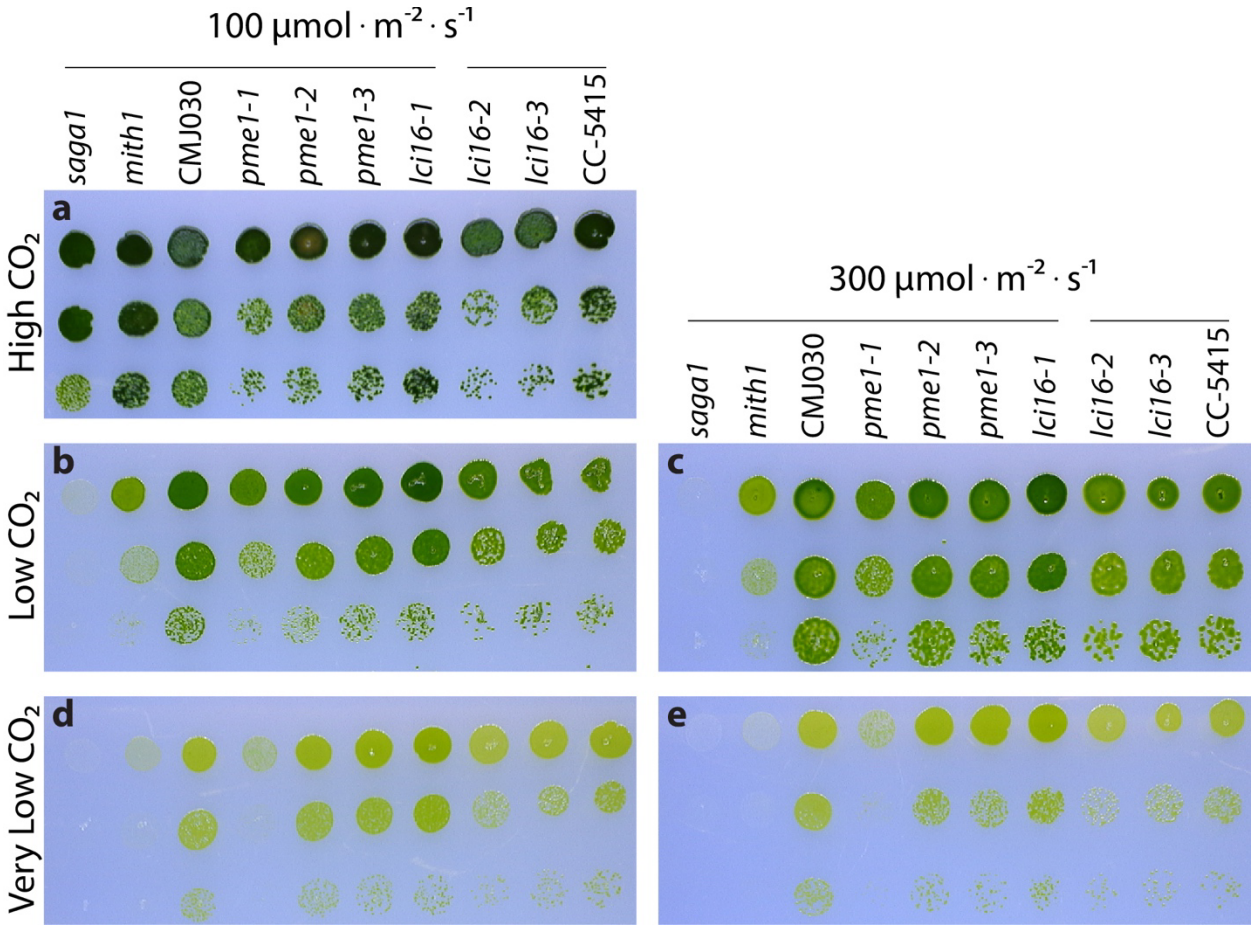

Figure 5: LCI16 and PME1 are not required for normal growth under CCM-inducing conditions

Spot tests of wild-type strains, *lci16* and *pme1* mutants, and known CCM mutants *saga1* and *mith1* under high (3%) **(a)**, low (~400 ppm) **(b-c)**, and very low (~40 ppm) **(d-e)** CO_2 conditions under 100 **(a,b,d)** and 300 **(c,e)** µmol · m^{-2} · s^{-1} of photons. All mutant strains are in the CMJ030 wild-type background strain except for *lci16-2* and *lci16-3*, which are in the CC-5415 background. Horizontal lines over the genotypes indicate strains that share the same wild-type background.

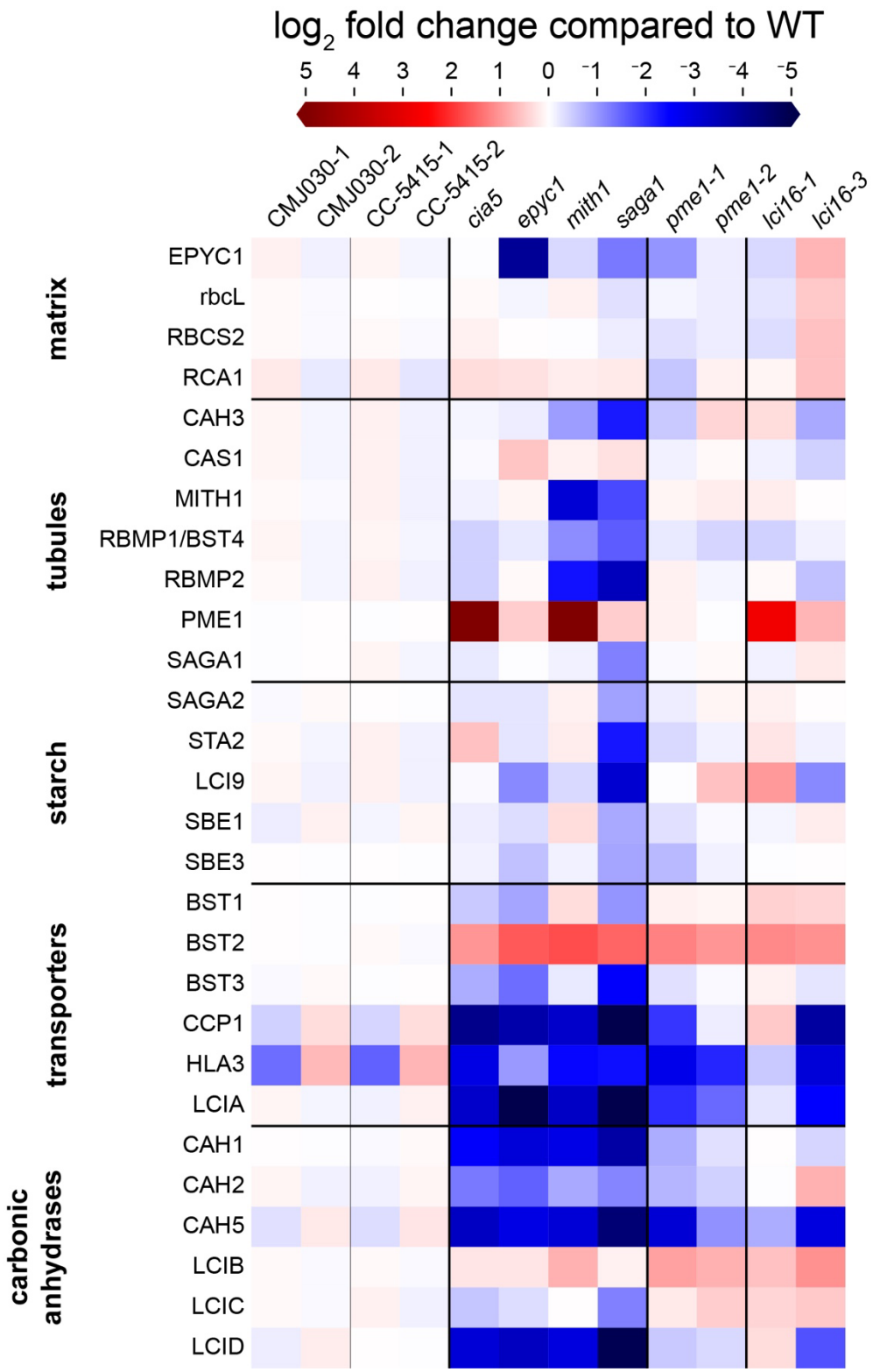

Figure 6: Comparison of CCM-related protein abundance in known CCM mutants and *lci16* and *pme1* mutants

891 Mass spectrometry was used to determine the whole-cell proteome of the known CCM mutants
892 *cia5*, *epyc1*, *mith1*, and *saga1*; two alleles each of *lci16* and *pme1*; and two biological replicates
893 of each strain's wild-type background (all strains are in the CMJ030 background except for
894 *lci16-3*, which is in the CC-5415 background). All strains were pre-cultured in TP high CO_2 (3%
895 CO_2), then diluted and shifted to low CO_2 levels (~400 ppm CO_2) for 16 hours prior to harvesting
896 for mass spectrometry. The heatmap shows the relative abundance of CCM-related proteins
897 (rows) in each genotype (columns), expressed as the $\log_2$ fold-change of each protein relative to
898 its wild-type parental strain (averaged between both biological replicates). Proteins are grouped
899 into localization- and function-based groups, denoted by horizontal black lines. Proteins that
900 were quantified based on only one peptide are excluded from the heatmap, but can be found,
901 along with the full dataset, in Supporting Information Datasets **S6-7**.

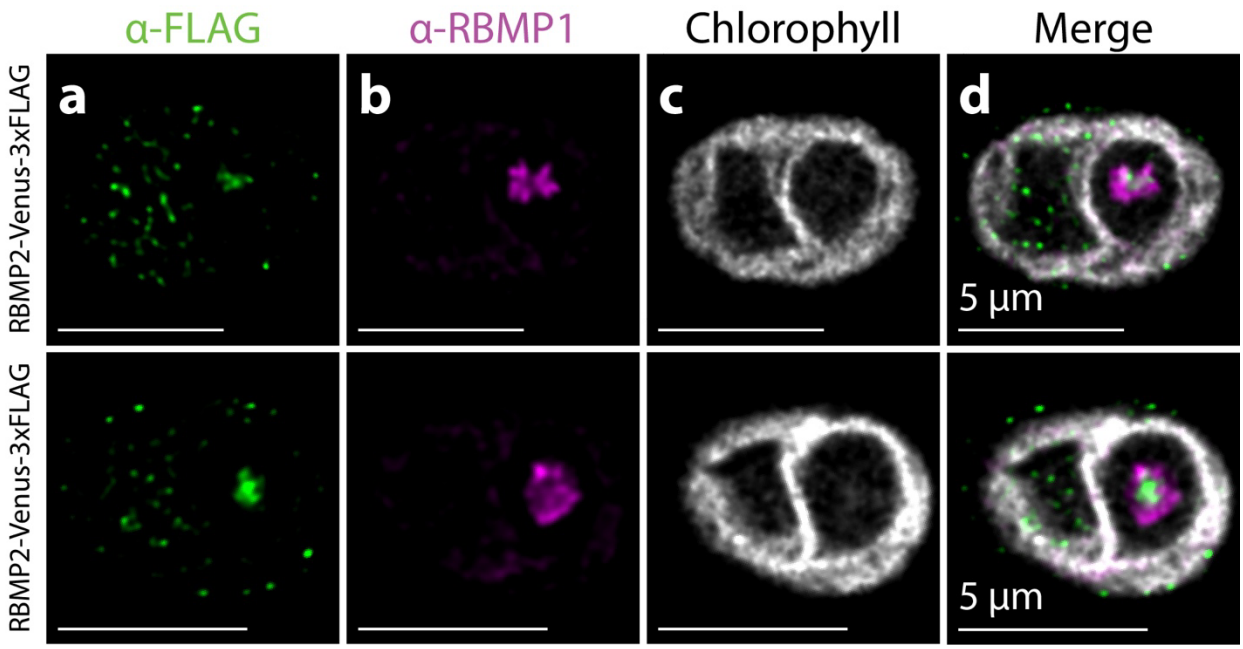

Supporting Information Figure S1: RBMP1 and RBMP2 localize to different regions of the pyrenoid tubules.

Wild-type cells expressing RBMP2-Venus-3×FLAG were immunostained using α-FLAG **(a)** and α-RBMP1 **(b)** antibodies. Each row represents an independent cell from the same RBMP2-Venus-3×FLAG strain. A gap in the chlorophyll signal **(c)** in the base of each cell (on the right side of each image) represents the location of the pyrenoid. Merging the channels **(d)** shows the distinct localization of RBMP1 and RBMP2.

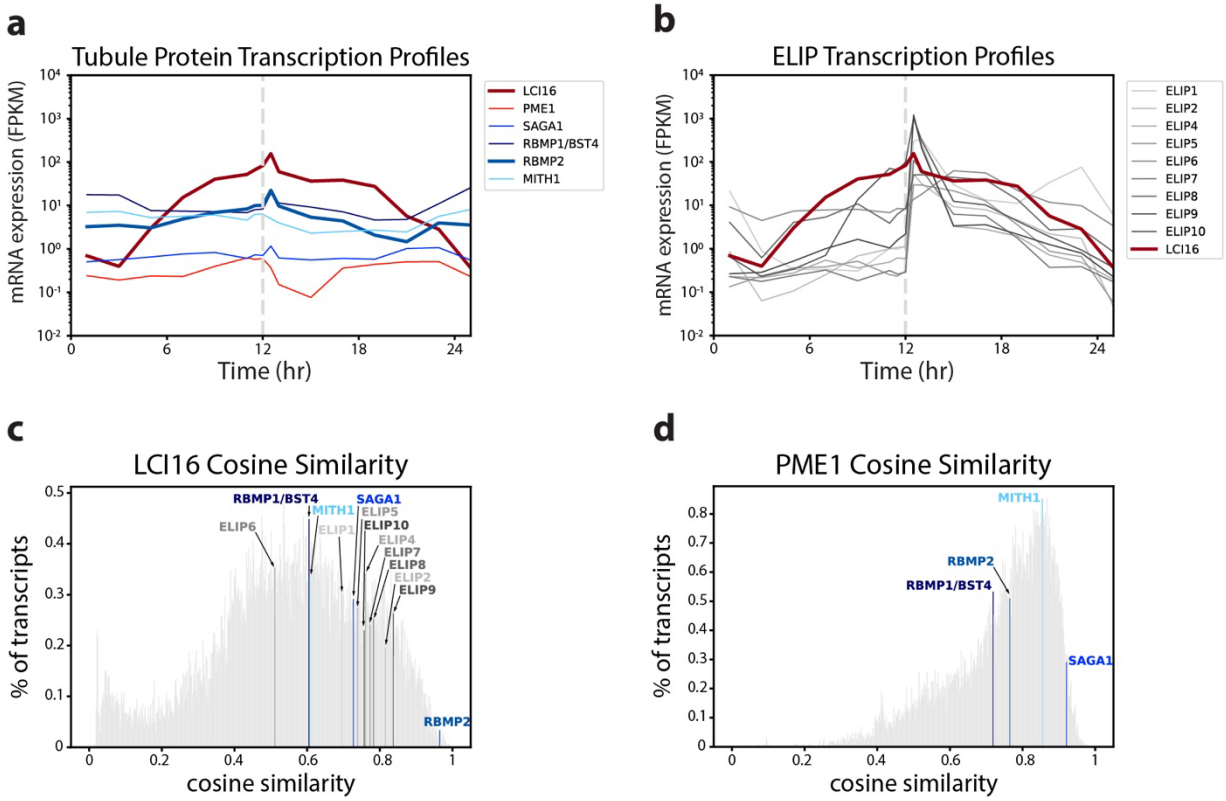

Supporting Information Figure S2: Comparison of LCI16's and PME1's expression profiles in diurnally-grown cells to the expression profiles of known tubule proteins and ELIP proteins

Plots showing transcriptomic and proteomic data from diurnally-grown *C. reinhardtii* cells measuring the abundance of mRNA (**a–b**) levels (Strenkert *et al.*, 2019) of known pyrenoid tubule proteins (blue lines; **a**) and the Early Light-Induced Proteins (ELIPs, grey lines; **b**) with which LCI16 shares homology. The transcription profile of LCI16 is shown in dark red in both panels. Hours 0 and 24 correspond to the onset of dark and hour 12 corresponds to the onset of light. (**c–d)** Histograms showing the cosine similarity of the Strenkert transcriptome profiles to the LCI16 (**c**) and PME1 (**d**) transcriptome profiles. The cosine similarity calculation considers each gene's transcription profile as a 16-dimensional vector (each dimension corresponding to one of the 16 timepoints measured) and measures the similarity between transcription profiles by calculating the cosine of the angle between the profiles' 16-D vectors. A cosine similarity of 1 corresponds to vectors that are parallel, i.e. identical transcriptome profiles. Note that because the angle between vectors is dependent on their direction, rather than their magnitude, this metric measures the similarity of the shape of the transcription profiles (i.e., which timepoints are up- and down-regulated), rather than the absolute transcript abundance at each timepoint. of Bins containing proteins known tubule proteins or ELIPs are colored as in panels **a–b**.

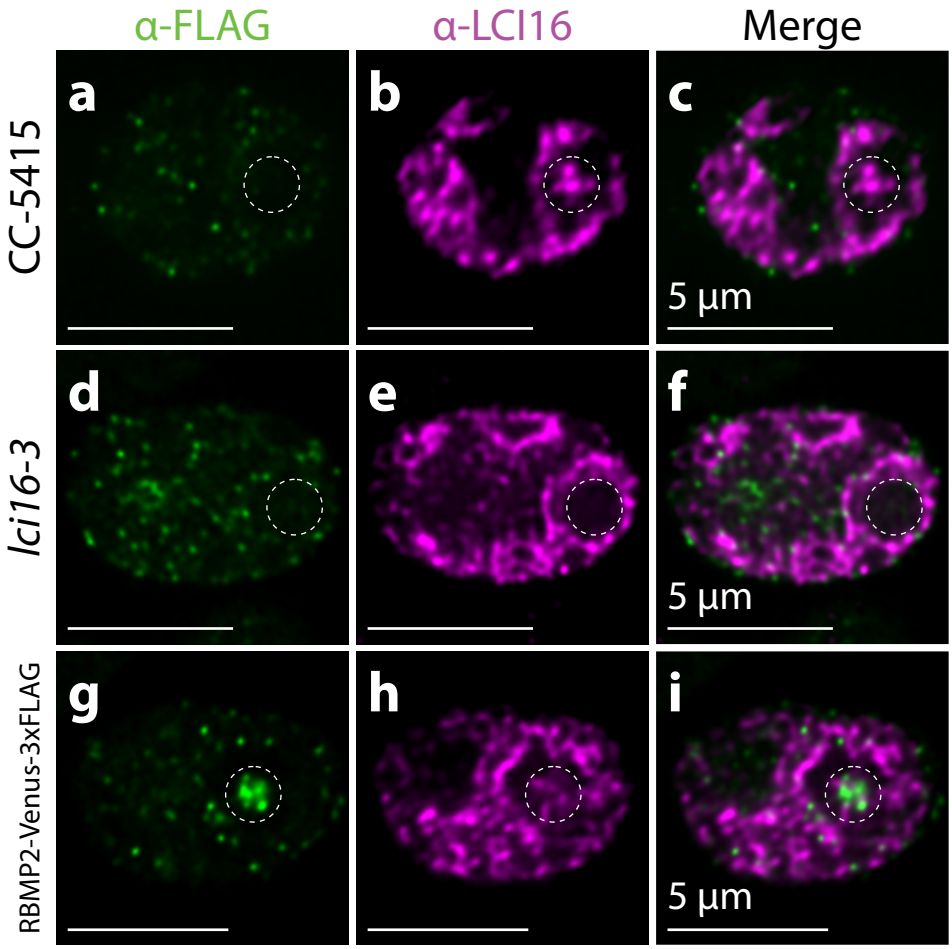

Supporting Information Figure S3: LCI16 antibody staining is non-specific but consistent with LCI16 tubule localization.

α-FLAG and α-LCI16 immunostaining in wild-type **(a-c)**, *lci16-3* **(d-f)**, and RBMP2-Venus-3xFLAG **(g-i)** cells. Pyrenoids are denoted with dashed circles. The α-LCI16 antibody stains the entire chloroplast, including the pyrenoid, in wild-type **(b)** and RBMP2-Venus-3xFLAG cells **(h)**. However, in the *lci16-3* mutant, the α-LCI16 signal is notably absent from the pyrenoid **(e)**.

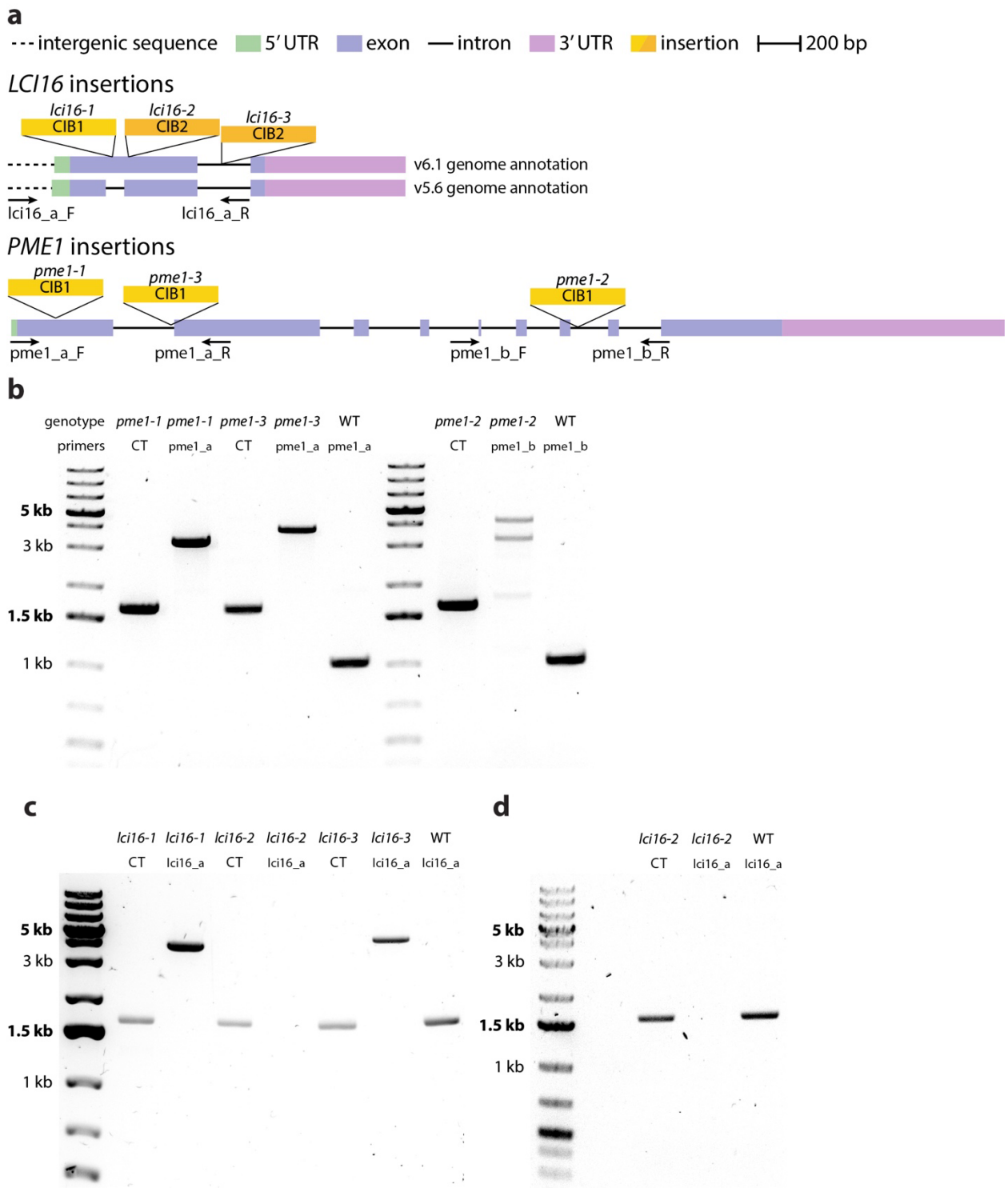

Supporting Information Figure S4: PCR verification of *lci16* and *pme1* insertional mutants

PCR verification of the insertions *lci16* and *pme1* mutants. (**a**) Maps of the LCI16 and PME1 genomic loci showing the locations of the CIB1 and CIB2 insertion cassettes and the primers used for PCR verification. The *lci16-1* insertion falls in a region that is annotated as an intron in

941 the v5.6 *C. reinhardtii* genome assembly and an exon in the v6.1 assembly—both gene models
942 are shown for clarity, but the insertional cassette should disrupt gene transcription regardless of
943 whether it is inserted in an exon or intron (Li *et al.*, 2019). Cassettes and primers are not drawn
944 to scale, but distances between them are to scale. Scale bar 200 bp. (**b-d**) Agarose gels
945 showing amplification across the insertion junction in genomic DNA purified from the *pme1* (**b**)
946 and *lci16* (**c–d**) mutants. Expected wild-type band lengths for each primer set can be found in
947 Supporting Information Table **S1**. For all strains except *lci16-2*, band lengths in excess of the
948 expected wild-type amplicon lengths were observed (**b-c**), indicating the presence of the
949 insertional cassette. The *lci16-2* gDNA failed to amplify using the insertion-spanning primers in
950 panel (**c**), though the successful amplification using the control (CT) primers confirmed the
951 presence of template gDNA. Panel **(d)** shows that the failure of the lci16_a primer pair to amplify
952 *lci16-2* gDNA in independent PCR reactions is reproducible. Such a reproducible failure to
953 amplify despite a working control is consistent with a very large insertion, and was taken as an
954 indication of a correct insertion, as previously done (Kafri *et al.*, 2023).

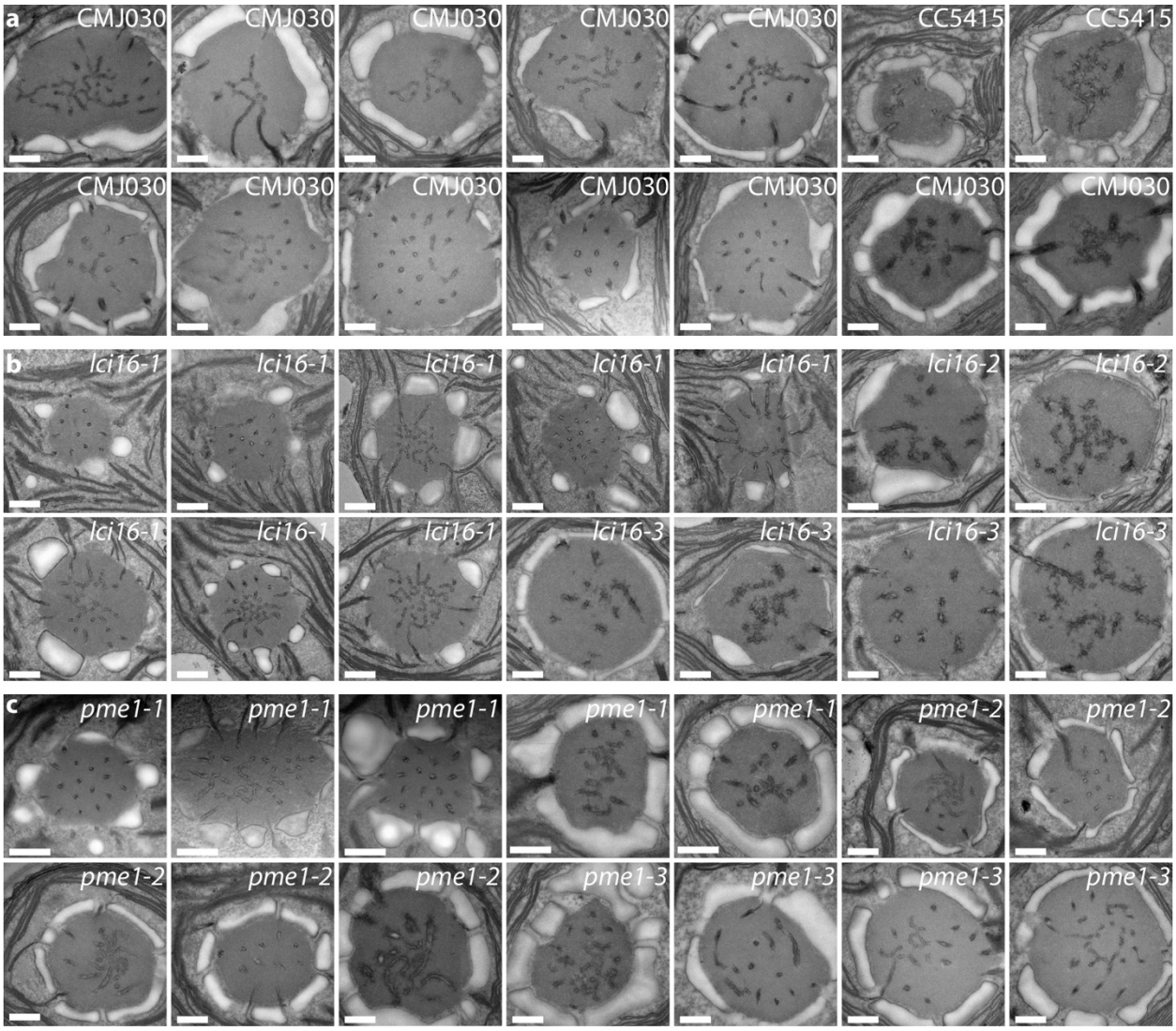

Supporting Information Figure S5: Additional TEM pyrenoid images of insertional mutants of *lci16* and *pme1*

Additional micrographs of wild-type (**a**), *lci16* (**b**), and *pme1* (**c**) pyrenoids, showing that lci16 and pme1 mutant pyrenoids contain central reticulated regions and minitubule-containing peripheral tubules. Scale bars 500 nm.

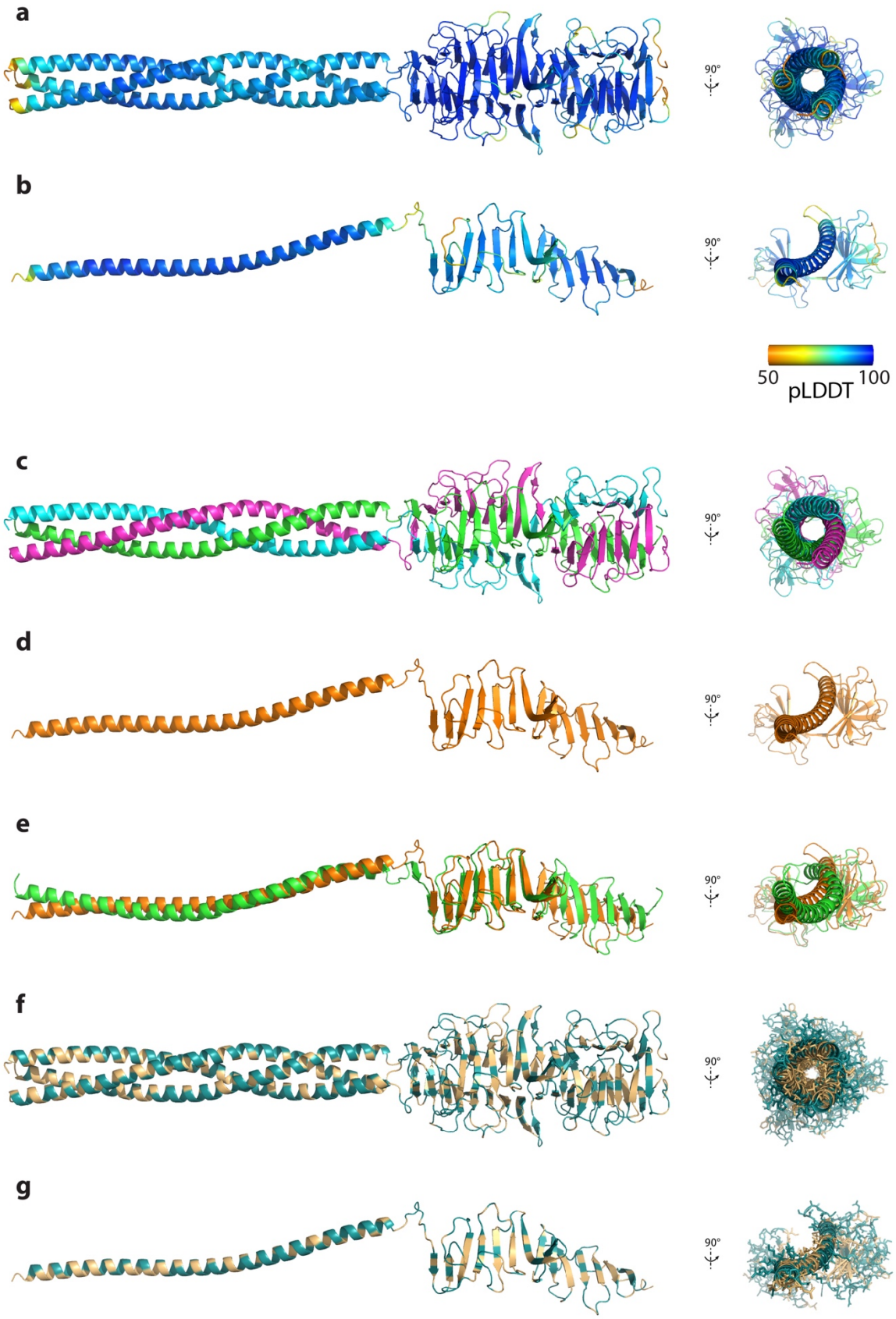

961

Supporting Information Figure S6: AlphaFold 3 predicts an amphipathic helix and beta sheet in PME1.

AlphaFold 3 predictions of a trimer **(a,c,f)** and monomer **(b,d,g)** of residues 380–639 of PME1, the 260 residues at its C-terminus. **a–b**. The trimer **(a)** and monomer **(b)** colored according to the per-atom confidence metric pLDDT. Confidence scores for the entire structure are higher for the trimer (pTM = 0.83, iPTM = 0.82) than the monomer (pTM = 0.49). **c–e.** Cartoon representation of the extended helix and beta sheet of the predicted trimer **(c)**, in which the helices form a coiled coil and the beta sheets form a beta-barrel-like structure, and the monomer **(d)**, which takes on a similar conformation even in the absence of oligomerization, as shown by an overlay of the monomer with one subunit of the trimer **(e)**. **f–g.** The predicted trimer **(f)** and monomer **(g)** colored by Kyte-Doolittle hydrophobicity (Kyte & Doolittle, 1982), with hydrophilic residues colored deep teal and hydrophobic residues colored beige. In the 90-degree rotations showing the structure along the axis of the helix, side chain visualization has been added to show that the interior of the coiled coil contains almost exclusively hydrophobic residues, while the exterior is almost entirely hydrophilic.

Primer name	Sequence	Strains tested	Expected amplicon length (bp)
CT_F	CGGTGATACTTACACGCCC	All	1867
CT_R	CACAGTTTGTGTGGAATCGG		
lci16_a_F	CAGGGGAGTAGCAAAACAG	*lci16-1*, *lci16-2*, *lci16-3*	1643
lci16_a_R	GCTGCTTCATGTGACCTTG		
pme1_a_F	CATAGAGCTTGCCATGTTATATCC	*pme1-1*, *pme1-3*	1025
pme1_a_R	AGAAGGAGACGAAAGCACAGG		
pme1_b_F	GGCTTGGATGACTGATGACCG	*pme1-2*	1014
pme1_b_R	ACCTCGCCAATGCACAGACG		

977 **Supporting Information Table S1: Primers used for PCR verification of *lci16* and *pme1***
978 **insertional mutants**